J. Fluid Mech. (1967), *vol.* 28, *part* 4, *pp.* 719–754
Printed in Great Britain

Wall-pressure fluctuations associated with subsonic turbulent boundary layer flow

By M. K. BULL

Department of Mechanical Engineering, University of Adelaide, South Australia

(Received 17 March 1964 and in revised form 18 July 1966)

Experimental results are given for various statistical properties of the fluctuating wall-pressure field associated with a subsonic turbulent equilibrium boundary layer, developed on a smooth wind tunnel wall after natural transition from laminar to turbulent flow.

The statistical quantities of the wall-pressure field investigated were root-mean-square pressure, frequency power spectrum and space–time correlations. Space–time correlation measurements were made in both broad and narrow frequency bands. The experiments were made at flow Mach numbers of 0·3 and 0·5 and covered a Reynolds number range of about 5 to 1.

The main conclusion to which the measurements lead is that the wall-pressure field has a structure produced by contributions from pressure sources in the boundary layer with a wide range of convection velocities, and comprises two families of convected wave-number components. One family is of high wave-number components and is associated with turbulent motion in the constant stress layer; the components are longitudinally coherent for times proportional to the times taken for them to be convected distances equal to their wavelengths and laterally coherent over distances proportional to their wavelengths. The other family comprises components of wavelength greater than about twice the boundary-layer thickness, which lose coherence as a group more or less independently of wavelength and are associated with large-scale eddy motion in the boundary layer, outside the constant stress layer. The evolution of the pressure field is discussed in terms of these two wave-number families.

1. Introduction

From the experimental point of view, our knowledge of pressure fluctuations in turbulent flows is not nearly as extensive as that of velocity fluctuations. This stems from the lack of a generally applicable pressure-measuring instrument which can be used in the same wide variety of circumstances as the hot-wire anemometer. Measurements of pressure fluctuations within a turbulent flow have been made in a few isolated cases—for example by Kobashi (1957) in wake flow and (indirectly) by Uberoi (1954) in isotropic turbulence—but it is only in the particular case of wall-pressure fluctuations produced by turbulent shear flow over a boundary surface, where a pressure transducer can be mounted in the surface without disturbing the flow in any way, that experimental data are becoming at all extensive. Interest in wall-pressure fluctuations has also been intensified because of the engineering problems they give rise to.

The earliest attempt at a theoretical treatment of pressure fluctuations in a turbulent shear flow was made by Kraichnan (1956*a*, *b*, 1957). He concluded that pressure fluctuations at a point are produced by quite local velocity fluctuations, and that the dominant contribution to the mean-square pressure is produced by the interaction between turbulence and mean shear except perhaps at low wave-numbers. He estimated the ratio of root-mean-square pressure p' to wall shear stress τ_W to be about 6. Using a similar type of analysis Lilley & Hodgson (1960) also found a dominance of turbulence/mean shear interaction and derived a value of about 3. The dominance of turbulence/mean shear interaction has, however, recently been questioned by Corcos (1962, 1963*b*).

Experimental measurements of wall-pressure fluctuations in shear flows influenced by solid boundaries have been reported by a number of investigators. Wall-pressure fluctuations due to turbulent boundary-layer flow have been investigated by Harrison (1958), Willmarth (1958, 1959), Bull (1960), Bull & Willis (1961), Willmarth & Wooldridge (1962), Hodgson (1962) and Serafini (1963), all working with air at subsonic speeds, by Kistler & Chen (1962), working with air at supersonic speeds, and by Skudrzyk & Haddle (1960) and Bull & Willis (1961) in the case of water flows. Pressure fluctuations at the wall of a pipe with fully developed turbulent flow have been measured by Corcos (1962) and by Bakewell *et al.* (1962) and beneath a wall jet by Lilley & Hodgson (1960).

Although there were fairly wide discrepancies among various investigators, early work on subsonic flows established the order of magnitude of the root-mean-square pressure fluctuation, the general form of the frequency spectrum, and the convected nature of the wall-pressure field. Perhaps the main criticism which can be made of this early work is that in almost all cases the size of the pressure transducer was too large in relation to the thickness of the boundary layer in which it was used. This resulted in attenuation of the pressure signal at high frequencies, due to the cancellation of small-scale components of the pressure field over the face of the transducer, and precluded any detailed examination of the small-scale components.

In the present experiments the first aim was to achieve a small value of the ratio of transducer diameter to boundary-layer thickness by using miniature pressure-sensing elements, in order to obtain more precise pressure measurements and to make possible the detection of any existing differences in the behaviour of large- and small-scale components. The second aim was to study the detailed structure of the pressure field by investigating the behaviour of the various frequency or wave-number components of which it is composed by correlation measurements on the pressure signals after they had been filtered into narrow frequency bands.

2. Pressure field scales

The choice of the scales (see also Corcos 1963*b*) to be used in the presentation of experimental data for a quantity such as the fluctuating wall pressure, which can receive contributions from pressure sources distributed throughout the boundary layer, is complicated by the fact that the representation of the dis-

tribution of mean velocity and turbulence intensities, at any streamwise station in a turbulent boundary layer, cannot be made in terms of the same velocity and length scales over the whole layer thickness, but requires a distinction between an inner (constant stress) region and an outer wake-like region. The outer region and the fully turbulent part of the constant stress layer exhibit self-preservation of mean velocity profile (in velocity defect form) and distribution of turbulence intensities. The scales of velocity and length are the friction velocity $U_\tau = (\tau_W/\rho_0)^{\frac{1}{2}}$ (where ρ_0 is free-stream density) and the boundary-layer thickness δ respectively. For the remainder of the constant-stress layer closer to the wall the appropriate scales are U_τ and ν/U_τ (where ν is the kinematic viscosity).

If the wall-pressure field receives significant contributions from pressure sources in both regions of the boundary layer, the various functions associated with it will obviously show Reynolds number dependence when expressed in terms of either the outer or the inner layer scales. Which scales minimize this dependence must be determined by experiment.

3. Experimental details

3.1. *The wind tunnel*

The experimental data which are presented were obtained from measurements made on the turbulent boundary layer developed, after natural transition from laminar to turbulent flow, on one of the ground and polished 9 in. walls of the subsonic test section of the 9 in. by 6 in. boundary-layer tunnel in the University of Southampton.

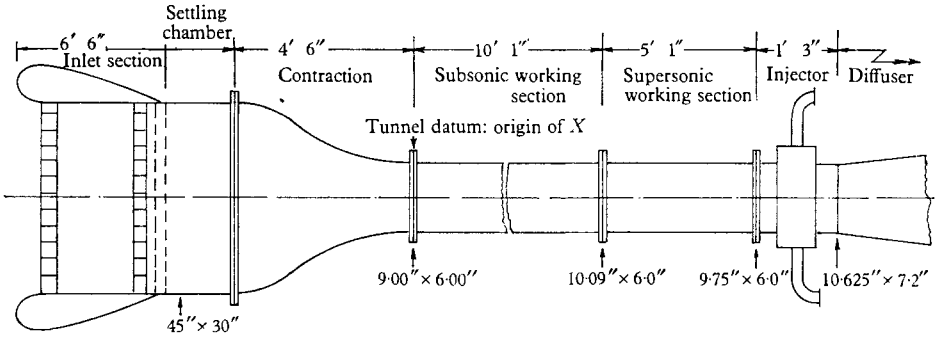

FIGURE 1. General arrangement of 9 in. × 6 in. boundary-layer wind tunnel.

This wind tunnel (figure 1) is of the induced-flow non-return type driven by the injection of compressed air downstream of the working sections. It has two working sections, a subsonic section 10 ft. long followed by a supersonic section 5 ft. long, both of which have rectangular cross-sections nominally 9 in. by 6 in. To keep vibration to a minimum, the working sections are of massive steel construction, and are mechanically isolated from the injector and from each other, being connected by flexible couplings. They are carried on flexible mountings which isolate them from vibration transmitted through the laboratory floor. The subsonic section is slightly divergent to compensate for boundary-

layer growth so that there is no pressure gradient along it. Instrumentation is mounted in 6 in. diameter plugs which fit ports in one of the 9 in. walls.

To keep the extraneous sound field in the test section to a minimum, the injector and diffuser are heavily sound-proofed, and in the present experiments the tunnel was always run in a choked condition so that injector noise and diffuser noise were not propagated internally into the test section. The diffuser outlet is outside the laboratory building.

3.2. *Instrumentation*

All measurements of fluctuating pressure were made with piezoelectric transducers mounted rigidly in the wind-tunnel wall. The face of the transducer and the wall formed a continuous surface. The pressure-sensitive elements were lead zirconate–titanate disks 0·029 in. diameter and 0·018 in. thick. The ratio of diameter of pressure-sensitive element d to boundary-layer displacement thickness δ^* lay in the range $0{\cdot}15 < d/\delta^* < 0{\cdot}51$ and was therefore considerably smaller than that achieved in most previous investigations.

An overall calibration and a check on the linearity and uniformity of frequency response were obtained from the response of the transducer to the passage across its face of shock waves of various strengths. A detailed low-frequency response for frequencies up to about 1000 c/s was obtained by calibration against a standard microphone, the two instruments being mounted in a small cavity, together with a moving-coil calibration signal generator (with this procedure the transducer could be calibrated in its experimental mounting). The calibration was normally checked before and after each tunnel run when root-mean-square pressure and spectral density measurements were being made.

The electrical output of the transducer was fed to a pre-amplifier with high input impedance, of the order of 5×10^8 ohm, and then further amplified for direct spectral analysis (Bruel and Kjaer $\frac{1}{3}$-octave Audio Frequency Spectrometer Type 2111) or for recording on magnetic tape (Ampex Model FR-100 tape recorder). All correlation values were obtained from recorded signals processed by the correlation equipment described by Allcock, Tanner & McLachlan (1962). For narrow-band correlations the signals in each replay channel were passed through $\frac{1}{3}$-octave filters before being fed to the correlator. The two channels were phase-matched in all cases.

Signals for correlation were recorded at a tape speed of 15 in./sec, but because of the limited bandwidth of the correlator ($0 < f < 12{,}000$ c/s), it was necessary to replay at reduced speed, 3·75 in./sec, in order to accommodate the bandwidth of the pressure fluctuation signals.

Velocity fluctuations were measured by means of a constant temperature hot-wire anemometer (Disa Type 55A01). The hot wires were of tungsten 0·0002 in. in diameter, electrically welded to their supporting needles. After welding, the wire and needle tips, with the exception of a 0·06 in. length at the centre of the wire which formed the working portion, were copper plated. The hot-wire probes were carried on supports of aerofoil section which could be traversed normal to the tunnel wall. The supports were designed to avoid significant increases in the sound pressure level in the tunnel working section.

3.3. *Scope of the measurements*

Measurements of mean-square pressure were made at nine streamwise stations at a free-stream Mach number M_0 of 0·3 and at ten stations at $M_0 = 0{\cdot}5$, those of frequency power spectral density and broad-band space–time correlation coefficient at two stations at $M_0 = 0{\cdot}3$ and three at $M_0 = 0{\cdot}5$, and those of narrow-band correlation coefficient at two stations at $M_0 = 0{\cdot}3$ and one at $M_0 = 0{\cdot}5$. Broad- and narrow-band correlation measurements were made for separation distances along lines making angles of $\beta = 0°$, 30°, 60° and 90° with the flow direction.

3.4. *Extraneous pressure signals and bandwidth limitations*

The amplified signal from the pressure transducer may contain extraneous contributions due to the sound field in the working section, inertia stresses resulting from vibration of the transducer, and electronic noise in the amplification system.

Of these the sound field in the working section was the main source of interference. Its intensity and spectrum were measured by means of a Bruel and Kjaer $\frac{1}{2}$ in. condenser microphone and cathode follower combination fitted with a nose fairing. Acoustic disturbances in the working section produced by the introduction of solid bodies such as Pitot tubes and hot-wire probes could be quantitatively detected by a microphone in the wall of the settling chamber upstream of the intake contraction. In this way it was established that the faired microphone itself produced no significant increase in the sound pressure level in the working section.

The sound pressure level was found to increase in the downstream direction. At $M_0 = 0{\cdot}3$ the mean-square acoustic pressure amounted to 1·6% of the measured mean-square pressure at the upstream end of the working section, increasing to 5·2% at the downstream end, while at $M_0 = 0{\cdot}5$ the corresponding values were 2·7 and 10·2%. The microphone signal had a broad-band character, the power spectral density being highest at low frequencies and falling off with increasing frequency. Because of the high spectral density of this background field at low frequencies, the spectral density measurements of the pressure field were rejected for frequencies less than 300 c/s. The recorded signals for correlation purposes were also attenuated at frequencies less than 300 c/s by making use of the response characteristics of the tape recorder.

Measurements of the spectrum of the output of the transducer when it was mounted in the tunnel wall but shielded from the flow showed that the spectral density of vibration pick-up was less than 0·01 times that obtained with the transducer exposed to the air flow, at all frequencies greater than 200 c/s, and that the total vibration signal was negligible in comparison with the overall pressure signal.

In general electronic noise in the amplification system did not amount to more than about 0·2% of the mean-square pressure and its effects on root-mean-square pressure and spectral measurements were negligible.

Thus all interference effects on frequency power spectral density and correlation measurements were removed by rejection of frequencies less than 300 c/s. This set the lower frequency limit for these measurements. The upper frequency limit for power spectral density measurements was set by the spectrometer used at 31,500 c/s and for correlation work by the tape recorder response at about 30,000 c/s. The bandwidths for these measurements therefore ranged from approximately $0{\cdot}017 < \omega\delta^*/U_0 < 1{\cdot}7$ for the thinnest boundary layer and highest speed investigated to $0{\cdot}071 < \omega\delta^*/U_0 < 7{\cdot}5$ for the thickest boundary layer and lowest speed investigated (where ω is the circular frequency, $2\pi f$, and U_0 the free-stream velocity).

For root-mean-square pressure measurements the bandwidth was determined by the response characteristics of the amplification system as $80 < f < 100{,}000$ c/s (equivalent to a variation from $0{\cdot}0044 < \omega\delta^*/U_0 < 5{\cdot}5$ for the lowest δ^* highest U_0 case to $0{\cdot}024 < \omega\delta^*/U_0 < 30$ for the highest δ^* lowest U_0 case). Since the bandwidth extended to frequencies below 300 c/s it was necessary to correct the results for acoustic interference.

Despite the miniature size of the pressure transducer elements, corrections had also to be applied to the root-mean-square and spectral density measurements for the limitations of transducer resolution.

For narrow frequency band measurements, convection velocities are not quoted for playback frequencies less than 250 c/s (true frequency 1000 c/s) because of the difficulty of obtaining no relative phase shift in the two replay channels at low frequencies. In the worst case this gives a limiting Strouhal number, $\omega\delta^*/U_0$, of about 0·24. In a few cases correlation coefficients are given for lower frequencies (down to 400 c/s true frequency); in such cases the associated convection velocities have been obtained from mean curves.

4. The flow under investigation

4.1. *Mean flow parameters*

The mean flow parameters were derived from total pressure measurements in planes normal to the free-stream direction and the corresponding static pressure at the boundary surface. Total pressures were measured by means of a Pitot tube and no corrections were applied to the measured values.

Two flow conditions were used. At the lower speed (generally referred to as the $M_0 = 0{\cdot}3$ condition) the free-stream conditions were essentially constant along the working section; the Mach number M_0 was 0·297, velocity $U_0 = 329$ ft./sec, and dynamic pressure $q_0 = 122$ lb./ft^2. At the higher speed (referred to as the $M_0 = 0{\cdot}5$ condition) there was a small variation along the test section in the downstream direction: $M_0 = 0{\cdot}496$ to $0{\cdot}493$, $U_0 = 542$ to 539 ft./sec, $q_0 = 306$ to 303 lb./ft^2.

The variation with the distance X along the test section of the displacement thickness δ^*, momentum thickness θ, and form parameter H $(= \delta^*/\theta)$ of the boundary layer and Reynolds number $Re_\theta = U_0\theta/\nu_0$ is shown in figure 2. Where values of the geometrical thickness of the boundary layer δ are required they have been obtained from the corresponding δ^* by means of the relation

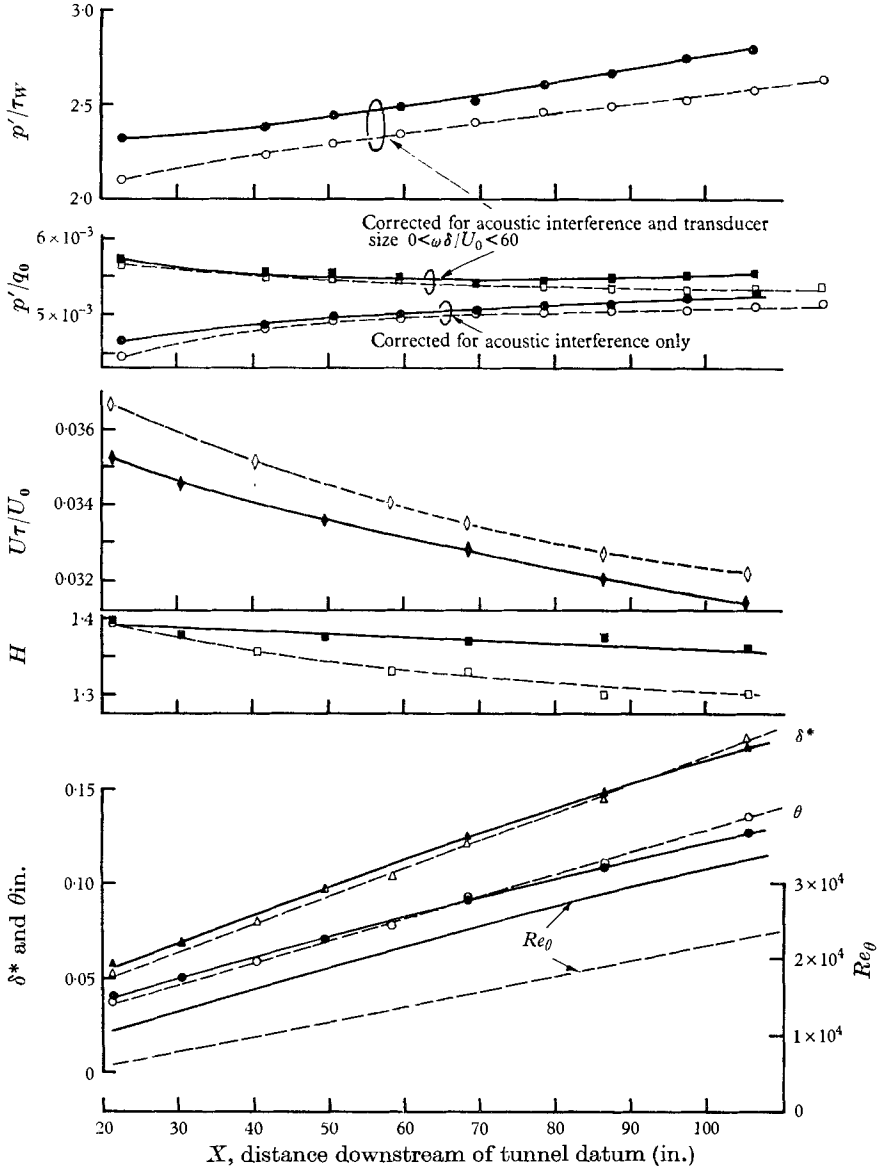

FIGURE 2. Boundary-layer parameters and root-mean-square pressure fluctuation. Variation with streamwise distance along test section. Open symbols and broken lines, $M_0 = 0{\cdot}3$; full symbols and unbroken lines, $M_0 = 0{\cdot}5$.

$\delta^*/\delta = 3{\cdot}88\,U_\tau/U_0$ corresponding to the equilibrium boundary layer of Coles (1956). The values of δ so obtained agree very well with the x_2 for which the experimental U_1/U_0 reach about 0·99. Figure 2 also shows values of skin friction velocity U_τ derived from the slopes of the profiles of mean velocity U_1 at small values of x_2 (the co-ordinate normal to the wall) using the 'law of the wall',

$$U_1/U_\tau = [\ln(x_2 U_\tau/\nu) + A]/K,$$

with the universal constant K equal to 0·40.

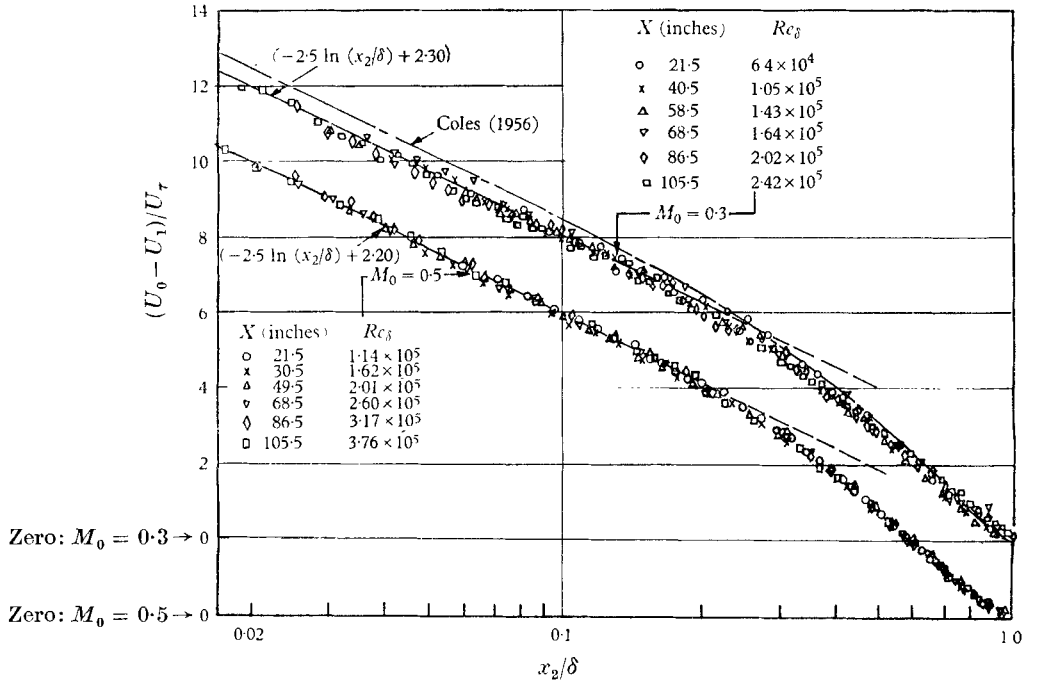

FIGURE 3. Boundary-layer mean velocity profiles.

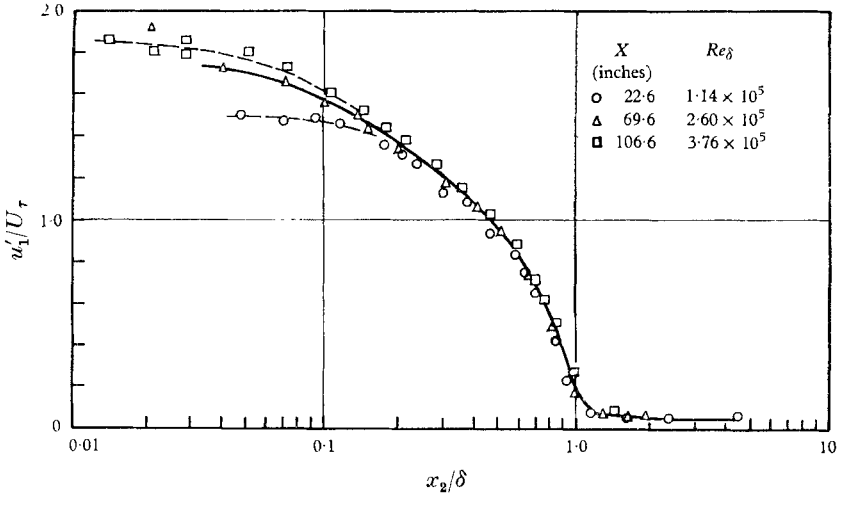

FIGURE 4. Profiles of intensity of longitudinal velocity fluctuations. $M_0 = 0{\cdot}5$.

The mean velocity profiles are plotted in velocity defect form in figure 3, which shows that over the outer region and part of the constant stress layer the boundary layer is exhibiting self-preservation of mean velocity profile. The equilibrium profile of Coles (1956) is included for comparison.

4.2. *Distribution of turbulence intensity*

The intensity of the longitudinal fluctuating velocity component u_1 was measured at three streamwise stations at $M_0 = 0{\cdot}5$. The results are shown in figure 4, where the ratio of root-mean-square velocity to skin friction velocity u_1'/U_τ is plotted against x_2/δ. Over the greater part of the boundary layer (x_2/δ greater than about 0·15) the results can be quite well represented by the self-preserving form

$$\langle u_1^2 \rangle = U_\tau^2 g_1(x_2/\delta),$$

(where $\langle\,\rangle$ denotes a time average) although even in this region there is some tendency for u_1'/U_τ to increase with increasing Reynolds number (by about 5 % over the Reynolds number range covered). However, the measurements of mean velocity profile and the longitudinal component of turbulence indicate that the boundary layer investigated approximated fairly closely to an equilibrium layer.

Over the inner part of the layer there is a strong influence of Reynolds number on u_1'/U_τ. This, of course, is to be expected in the region of transition from outer layer similarity to wall similarity. If the data for this region (which do not extend to $x_2 U_\tau/\nu$ less than 160) are plotted against $x_2 U_\tau/\nu$ they appear to form a quite consistent extension of the data obtained by Laufer (1954) for the region $0 < x_2 U_\tau/\nu < 90$ of turbulent pipe flow.

The residual value of turbulence intensity in the free stream showed very little variation along the length of the working section, the mean value for $M_0 = 0{\cdot}5$ being $u_1'/U_0 = 2{\cdot}5 \times 10^{-3}$. No measurement of intensity was made for the free-stream condition $M_0 = 0{\cdot}3$.

The maximum values of sound pressure level measured by the faired microphone in the free stream in the working section were 112 dB (relative to 2×10^{-4} dyne/cm^2) and 123 dB at free-stream Mach numbers of 0·3 and 0·5 respectively. If the sound field consisted entirely of plane waves propagating in one direction the equivalent values of the ratio of root-mean-square acoustic velocity perturbation to free-stream velocity would be $1{\cdot}8 \times 10^{-4}$ and $4{\cdot}1 \times 10^{-4}$ respectively. Comparison of these values with the measured intensity of free-stream turbulence indicates that the velocity fluctuations in the free stream are predominantly vorticity fluctuations.

5. Broad-band measurements and frequency power spectrum

5.1. *Statistical quantities measured*

The broad-band measurements were all particular cases of the double pressure space–time correlation function or covariance of the pressure fluctuation at the point $\mathbf{x}$ at time t and that at point $\mathbf{x}+\boldsymbol{\xi}$ at time $t+\tau$,

$$Q_{pp}(\mathbf{x}, t;\, \mathbf{x}+\boldsymbol{\xi}, t+\tau) = \langle p(\mathbf{x}, t)\, p(\mathbf{x}+\boldsymbol{\xi}, t+\tau) \rangle,$$

where in the present case of wall measurements $\mathbf{x}$ and $\boldsymbol{\xi}$ are vectors confined to the plane of the boundary surface and $\langle\,\rangle$ denotes a time average.

If, as in the case of a slowly growing boundary layer, the pressure field can be considered to be homogeneous and stationary in time, the correlation function is a function of spatial separations and time differences only and can then be denoted by $Q_{pp}(\xi_1, \xi_3, \tau)$, where ξ_1 and ξ_3 are the components of the separation vector in the streamwise (x_1) and cross-stream (x_3) directions respectively and τ is the time delay.

The only measurements of the correlation function in its dimensional form were for the particular case of the mean-square pressure

$$\langle p^2 \rangle = p'^2 = Q_{pp}(0, 0, 0).$$

The frequency power spectral density $\phi_p(\omega)$ of the pressure fluctuations was obtained by direct spectral analysis rather than via the autocorrelation $Q_{pp}(0, 0, \tau)$ (although measurements of $Q_{pp}(0, 0, \tau)$ were used to check direct spectral measurements in one or two cases). The two are related by the Fourier transforms

$$\phi_p(\omega) = \frac{2}{\pi} \int_0^\infty Q_{pp}(0, 0, \tau) \cos \omega\tau \, \mathrm{d}\tau,$$

$$Q_{pp}(0, 0, \tau) = \int_0^\infty \phi_p(\omega) \cos \omega\tau \, d\omega.$$

All other broad-band measurements concerned the correlation coefficient

$$R_{pp}(\xi_1, \xi_3, \tau) = Q_{pp}(\xi_1, \xi_3, \tau)/Q_{pp}(0, 0, 0).$$

5.2. *Root-mean-square pressure and frequency power spectrum*

The measured frequency power spectral densities are shown in the form

$$\phi_p(\omega) \, U_0/q_0^2 \delta^*$$

against $\omega\delta^*/U_0$ in figure 5. Attenuation due to the finite size of the pressure-sensing element, more severe the higher d/δ^*, is evident at high frequencies.

By representing the cross-spectral density or narrow-band correlation as a function of the similarity variables $\omega\xi_1/U_c(\omega)$ and $\omega\xi_3/U_c(\omega)$, Corcos (1963*b*) has calculated transducer resolution corrections to frequency power spectral density in terms of $\omega r/U_c(\omega)$ (r = radius of pressure-sensitive element). Since the present narrow-band correlations are very similar to those assumed by Corcos, his data have been used directly with the frequency-dependent convection velocity $U_c(\omega)$ taken from figure 15. (In general the values of $\omega r/U_c$ are small enough for there to be little difference between the values given by Corcos's method and those found experimentally by Willmarth & Roos 1965.) The corrected spectral data even when expressed in terms of the wall shear stress and boundary-layer thickness in the form $\phi_p(\omega) \, U_0/\tau_W^2 \, \delta$ against $\omega\delta/U_0$ do not lie on a universal curve, the spectral density increasing slowly with Reynolds number at a given non-dimensional frequency. However, the shapes of the curves are accurately similar, as shown by figure 5, where τ_W^2 has been replaced by (corrected) $\langle p^2 \rangle$.

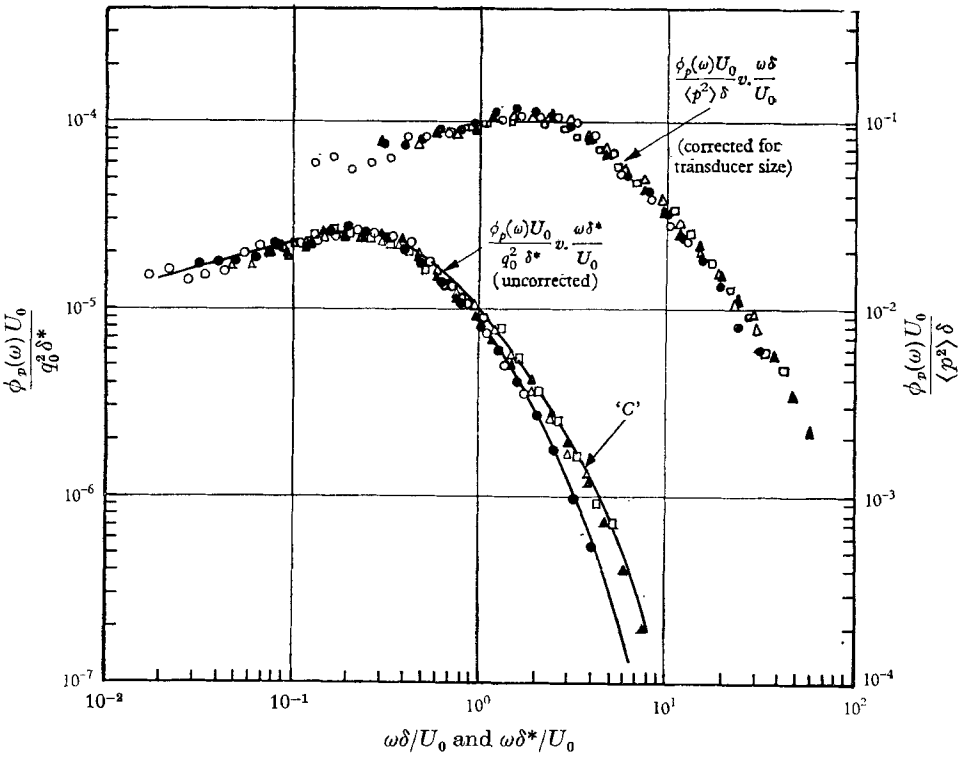

FIGURE 5. Frequency spectra of wall-pressure fluctuations.

	M_0	U_0 (in./sec.)	δ (in.)	δ^* (in.)	d/δ^*
●	0·3	3954	0·618	0·081	0·36
▲	0·3	3951	1·188	0·149	0·19
○	0·5	6502	0·431	0·057	0·51
△	0·5	6483	0·987	0·126	0·23
□	0·5	6468	1·425	0·173	0·17

The root-mean-square pressure fluctuation data are shown in figure 2. The variations of p'/q_0 and p'/τ_W with a streamwise distance along the working section, with corrections for background sound field and transducer resolution, are given. Resolution corrections were obtained as follows. The corrected value of p'/τ_W for the case in which the spectral measurements extended to the highest non-dimensional frequency ($M_0 = 0{\cdot}3$, $\delta = 1{\cdot}188$ in., for which $0{\cdot}60 < \omega\delta/U_0 < 60$) was obtained by integration of the spectrum. p'/τ_W for each of the other sets of spectral measurements was obtained from this value in proportion to the square roots of the ordinates of the corrected spectral curves making use of the similarity in shape noted above (and so avoiding integration of spectral curves over limited non-dimensional bandwidths). Hence the variation of the ratio of corrected to measured root-mean-square pressure p'/p_m with d/δ (figure 6) was obtained. Corrections for all other conditions were based on this curve. The results apply essentially for $0 < \omega\delta/U_0 < 60$. The magnitude of the corrected

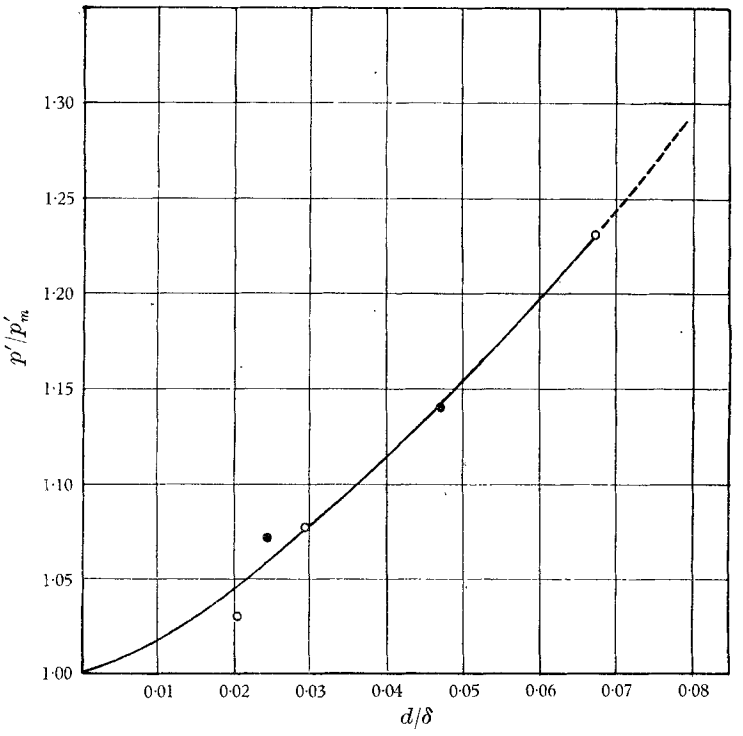

FIGURE 6. Correction to root-mean-square pressure fluctuation as a function of transducer size. ●, $M_0 = 0{\cdot}3$; ○, $M_0 = 0{\cdot}5$.

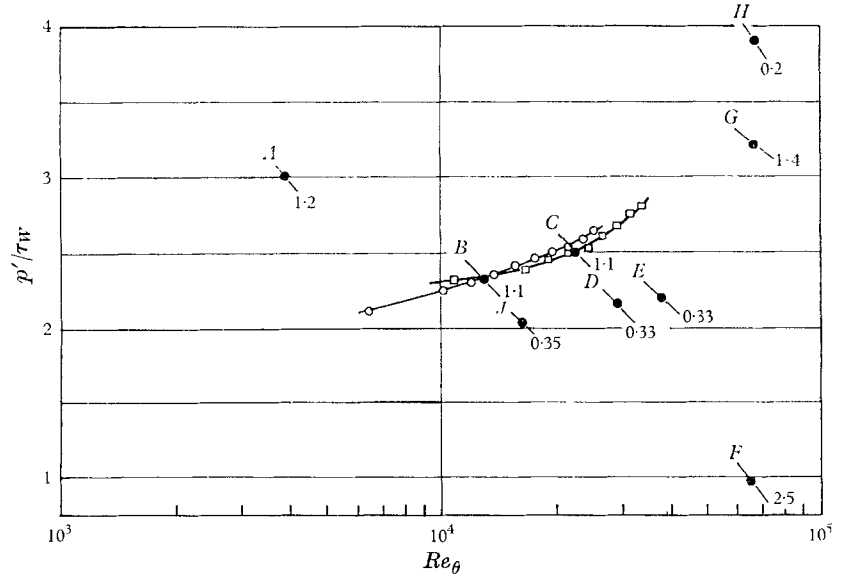

FIGURE 7. Variation of p'/τ_W with Reynolds number. *A*, Harrison (1958); *B* and *C*, Willmarth (1959); *D* and *E*, Willmarth & Wooldridge (1962); *F*, Skudrzyk & Haddle (1960); *G* and *H*, Serafini (1963); *J*, Bull & Willis (1961). Present tests corrected for transducer size: –○–, $M_0 = 0{\cdot}3$; –□–, $M_0 = 0{\cdot}5$. Numbers indicate value of d/δ^*.

spectral density at $\omega\delta/U_0 = 60$ indicates that higher frequencies make a significant contribution to p'. Thus the corrected values of p'/τ_W should be somewhat higher than the values given, but it is not possible to extimate by how much (the corrections used are in fact slightly less than the experimental values given by Willmarth & Wooldridge 1963).

The variation of the corrected values of p'/τ_W with Reynolds number Re_θ and comparison with other data are shown by figure 7. In addition to the data shown we have two values of p'/τ_W obtained by extrapolating data measured with transducers of various sizes to $d/\delta^* = 0$; Hodgson (1962) found $p'/\tau_W = 2{\cdot}2$ (from data covering an Re_θ range of roughly 1000 to 15,000) and Willmarth & Roos (1965) found $p'/\tau_W = 2{\cdot}66$ at $Re_\theta = 38{,}000$. (Note also that Willmarth & Roos give a revised value corresponding to point E of figure 7.) For the present results p'/τ_W increases from 2·11 at $Re_\theta = 6{,}400$ ($M_0 = 0{\cdot}3$) to 2·80 at $Re_\theta = 33{,}800$ ($M_0 = 0{\cdot}5$) at the rate of about the 0·17 power of Reynolds number. This trend contrasts with the results found by Corcos (1962) and by Bakewell *et al.* (1962) for fully developed pipe flow, since both of these investigations showed a systematic decrease in p'/τ_W with increasing Reynolds number. In §4.2 it was noted that the value of u_1'/U_τ over the outer part of the boundary layer ($x_2/\delta > 0{\cdot}15$) showed a small increase with increasing Reynolds number. If this effect is not due to experimental errors or uncertainties in determining δ, and it is taken as indicative of an increase in intensity of all turbulence components, it could account for an increase in p'/τ_W of from 5 to 10 % (depending on the relative importance of turbulence-turbulence interactions and turbulence/mean shear interactions in determining p'). However, it does not seem sufficient to account for the whole of the observed increase in p'/τ_W, which is about 21 % over the same range of Reynolds number. The other boundary-layer data (figure 7) do little either to support or to oppose the trend shown by the present results, suggesting only that if all results were corrected to zero size of pressure transducer (which would reduce the existing scatter) the effect of Reynolds number over the range

$$3000 < Re_\theta < 100{,}000$$

would not be large.

From the autocorrelation the integral time scale of the pressure field, defined as

$$\tau_\Lambda = \int_{-\infty}^{\infty} |\, R_{pp}(0, 0, \tau)\,| d\tau,$$

can be obtained. Use of the autocorrelation corresponding to the spectral curve C of figure 5, which is virtually free from transducer resolution effects and which is given by

$$\phi_p(\omega)\, U_0/q_0^2\delta^* = \{3{\cdot}7\exp(-2\tilde{\omega}) + 0{\cdot}8\exp(-0{\cdot}47\tilde{\omega}) - 3{\cdot}4\exp(-8\tilde{\omega})\}\, 10^{-5}, \quad (1)$$

where $\tilde{\omega} = \omega\delta^*/U_0$, leads to $\tau_\Lambda U_0/\delta^* = 3{\cdot}84$. In terms of δ/U_0, which the similarity of frequency power spectra indicates is the more appropriate time scale, the corresponding value is $\tau_\Lambda U_0/\delta \simeq 0{\cdot}47$. The value of the integral time scale $\int_{-\infty}^{\infty} R_{pp}(0, 0, \tau)\, d\tau$ (which is equal to $\pi\phi_p(0)/\langle p^2\rangle$) is $1{\cdot}10\,\delta^*/U_0$.

5.3. *Broad-band space correlations*

The experimental broad-band space correlations $R_{pp}(\xi_1, \xi_3, 0)$ are shown in figure 8 as a function of spatial separation divided by δ^*. A good collapse of data for the various flow conditions is obtained in this way. The experimental points are most numerous at spatial separations for which the correlation coefficient and the slope of the mean curve have fairly small values and in view of the inevitable experimental scatter it is not really possible to distinguish between δ^* and δ as length scales.

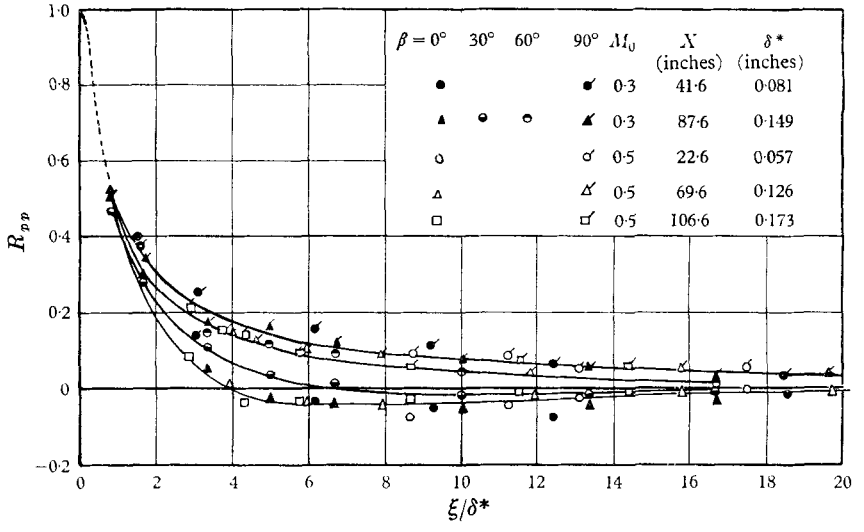

FIGURE 8. Space correlations of the wall-pressure field, $R_{pp}(\xi \cos\beta, \xi \sin\beta, 0)$ at various angles to the flow direction.

The longitudinal correlation curve becomes and remains negative for spatial separations greater than $\xi_1/\delta^* = 3{\cdot}9$, while the lateral correlation remains positive at all values of ξ_3/δ^* up to the largest at which measurements were made. The curves for the intermediate angles have intermediate forms. That for $\beta = 30°$ has a zero crossing at $\xi/\delta^* = 7$ while that for $\beta = 60°$ remains positive.

Longitudinal correlations have been measured previously by Willmarth & Wooldridge (1962) and by Hodgson (1962). Hodgson's measurements were restricted to separations $> 6\delta^*$ and there they show negative values of correlations very similar to the present results. In contrast, Willmarth & Wooldridge obtained positive values for all separations up to about $12\delta^*$. The negative values of longitudinal correlation at large separations obtained in the present investigation are believed to be real, and a reflexion of the fact that the frequency power spectral density falls off with decreasing frequency for $\omega\delta^*/U_0$ less than about 0·2. (Hodgson's results for the pressure spectrum on the wing of a glider show a greater fall-off at low frequencies than the present results and the negative loop on the spatial correlations is slightly larger.) The low-frequency cut-off at 300 c/s (see §3.4) could also produce this effect but calculations show that in general its

contribution is negligible. In the worst case it would make the minimum value of R_{pp} more negative by no more than 0·02.

The present lateral correlation values are slightly higher than those of Willmarth & Wooldridge for $0 < \xi_3/\delta^* < 8$ while for $\xi_3/\delta^* > 8$ the two sets of data are almost identical.

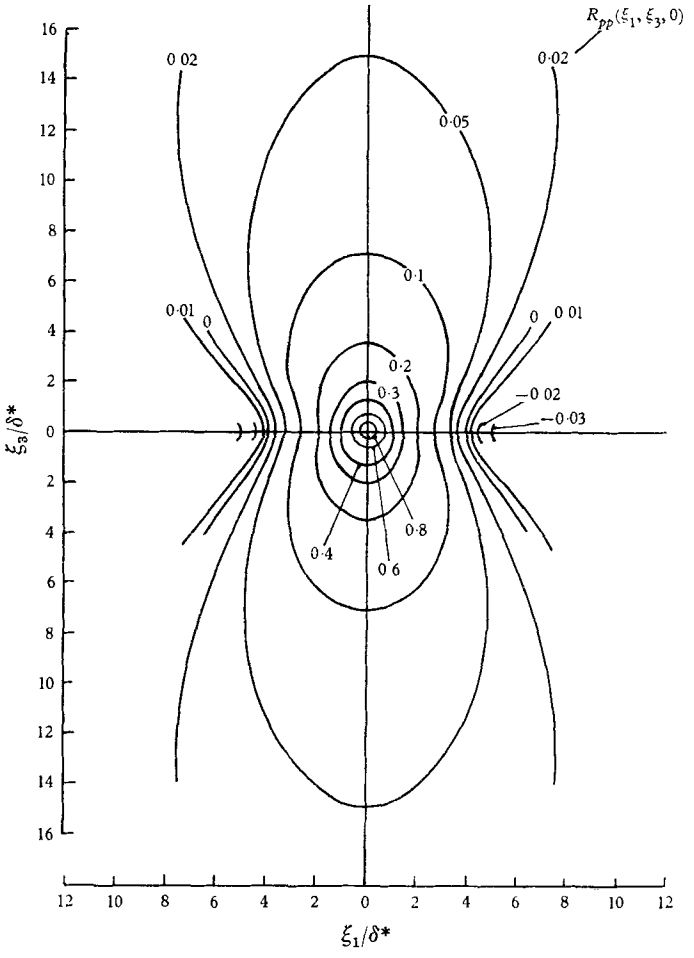

FIGURE 9. Contours of constant space correlation, $R_{pp}(\xi_1, \xi_3, 0)$ of the wall-pressure field.

From the space correlations for the four angles to the flow, the correlation pattern of the pressure field can be mapped out as a set of isocorrelation contours as in figure 9. The resulting pattern shows that at small spacings the field appears to be very nearly isotropic. The longitudinal and lateral micro scales (which are equal to the radii of curvature of the appropriate space correlation curves at zero separation) cannot be determined accurately from the experimental data because there are few points at small separations and because of transducer resolution errors which have the greatest effect on the fine scale motion. The data indicate upper limits on these scales of roughly $0{\cdot}5\delta^*$ or $0{\cdot}06\delta$. As spatial

separation increases anisotropy develops, the scale in the lateral direction exceeding that in the longitudinal direction. The longitudinal integral scale

$$(\Lambda_1)_{pp} = \int_{-\infty}^{\infty} |R_{pp}(\xi_1, 0, 0)| d\xi_1$$

is found to be $3{\cdot}20\delta^*$ or about $0{\cdot}40\delta$. The lateral integral scale $(\Lambda_3)_{pp}$ defined similarly has the value of $6{\cdot}74\delta^*$ or about $0{\cdot}84\delta$. We thus have

$$(\Lambda_3)_{pp}/(\Lambda_1)_{pp} = 2{\cdot}10.$$

In an incompressible flow, the wall-pressure correlation should satisfy the boundary condition, derived by Phillips (1954) and Kraichnan (1956*b*), that the integral area scale

$$\int_{-\infty}^{\infty} \int R_{pp}(\xi_1, \xi_3, 0)\, d\xi_1 d\xi_3$$

be zero, and should therefore be negative over parts of the field. Although negative values of correlation are observed, the experimental data do not satisfy this condition; the value of the ratio

$$\iint R_{pp}(\xi_1, \xi_3, 0)\, d\xi_1 d\xi_3 \Big/ \iint |R_{pp}(\xi_1, \xi_3, 0)| d\xi_1 d\xi_3$$

obtained by integration over a circle of radius $20\delta^*$ (the limit of the experimental data) is about 0·5. Three possible reasons why the measured integral scale is not zero are that, first, the negative area required for balance may be contributed by small negative values of R_{pp} at large ξ ($> 20\delta^*$); secondly, that the experimental measurements of small correlation values are not sufficiently accurate; and thirdly, that extraneous effects such as the background sound field in the wind tunnel have not been entirely removed by high-pass filtering and are causing the correlations at the larger separations to have more positive values than they otherwise would.

Theoretical work by Kraichnan (1956*b*, 1957) and later by Hodgson (1962) on particular models of boundary-layer flow indicates that if the wall-pressure field is mainly the result of interaction between the turbulence and the mean shear (through the pressure-source term $(\partial U_1/\partial x_2)(\partial u_2/\partial x_1)$), then the correlation should satisfy the additional boundary condition that the longitudinal integral scale

$$\int_{-\infty}^{\infty} R_{pp}(\xi_1, 0, 0)\, d\xi_1$$

and the integral time scale

$$\int_{-\infty}^{\infty} R_{pp}(0, 0, \tau)\, d\tau$$

be almost zero. Hodgson also showed that the lateral correlation $R_{pp}(0, \xi_3, 0)$ should be positive at all ξ_3. The observed correlations are qualitatively in agreement with these predictions, but the integral scales are not zero—the ratio

$$\int_{-\infty}^{\infty} R_{pp}(\xi_1, 0, 0)\, d\xi_1 / (\Lambda_1)_{pp}$$

is about 0·4 and $$\int_{-\infty}^{\infty} R_{pp}(0,0,\tau)\,d\tau/\tau_{\Lambda}$$

about 0·29. The reasons for the area scale not vanishing are relevant here also, and suggest that the values of the experimental integral scales should be closer to zero.The data therefore support the conclusion of Kraichnan and Hodgson that a large part of the mean-square pressure results from the interaction of turbulence and mean shear. The same conclusion has been drawn also by Willmarth & Wooldridge (1963) from their measurements of pressure–velocity correlations.

5.4. *Broad-band space–time correlations and convection velocities*

All the space–time correlation measurements made in the present series of experiments, for the various flow conditions and for the spatial separation in various directions to the flow, can be found elsewhere (Bull, Wilby & Blackman 1963) as sets of curves of correlation coefficient $R_{pp}(\xi_1, \xi_3, \tau)$ against the non-dimensional time delay $U_0\tau/\delta^*$ at various constant values of spatial separation. Here only one typical set of correlation curves is given (figure 10).

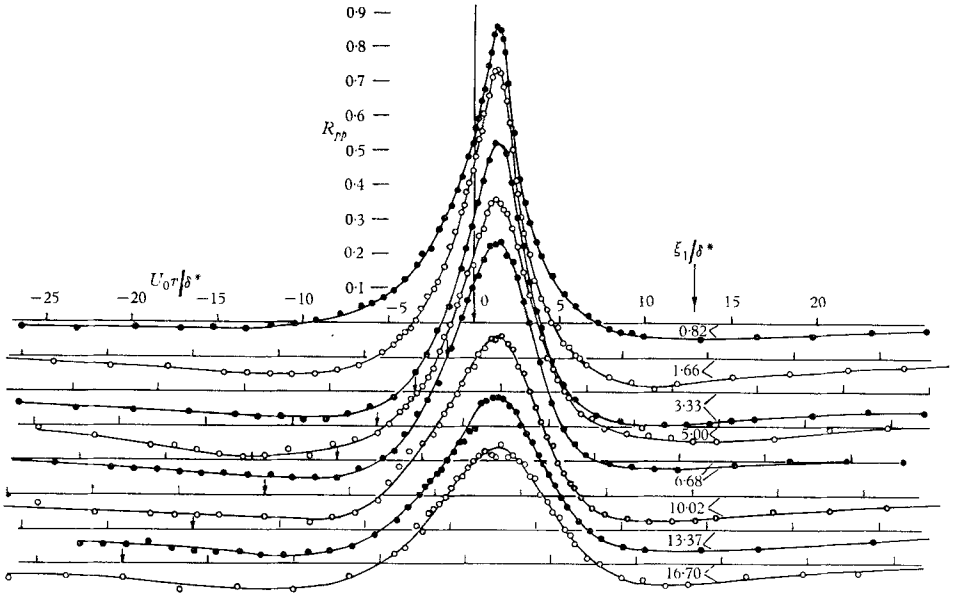

FIGURE 10. Typical longitudinal space–time correlations of the wall-pressure field, $R_{pp}(\xi_1, 0, \tau)$. $M_0 = 0{\cdot}3$, $\delta^* = 0{\cdot}149$ in., $X = 87{\cdot}6$ in. (arrows indicate locations of origins).

The space–time correlation curves for separations in the streamwise direction (for example figure 10) clearly have the character which would be associated with a convected pressure field slowly losing its coherence as convection proceeds. Whereas to an observer at a fixed point the pressure would appear coherent only for short times, to an observer who moved with the field so as to be always at the position of maximum correlation the field would appear to lose coherence quite slowly.

The variation with ξ_1 of τ_c, the time delay for which the ξ_1 = constant curve of $R_{pp}(\xi_1, 0, \tau)$ against τ touches the envelope of all such curves, defines the space–time path of a moving reference frame relative to which the rate of decay of the pressure correlation is a minimum at any given time delay. This path is shown

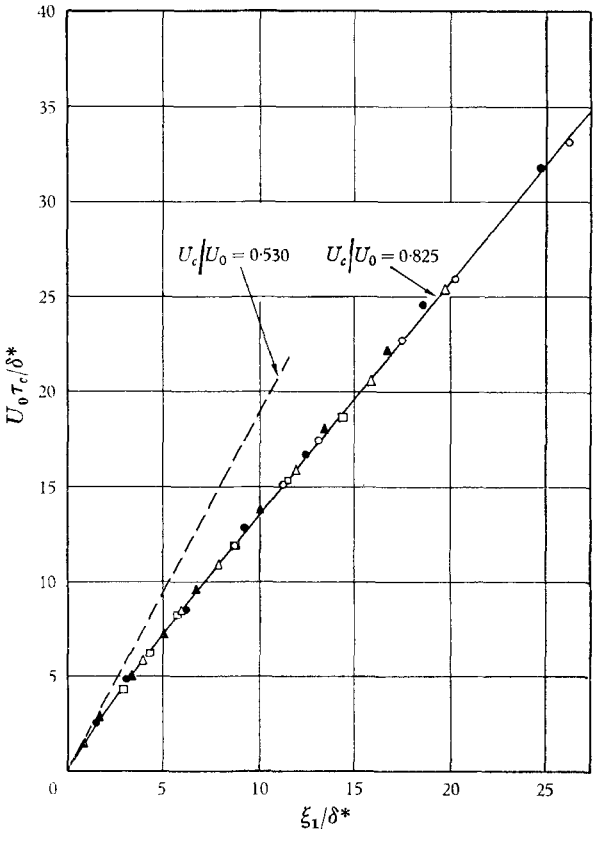

FIGURE 11. Space–time path of reference frame giving minimum decay rate of the pressure correlation.

	M_0	X	δ^*
●	0·3	41·6	0·081
▲	0·3	87·6	0·149
○	0·5	22·6	0·057
△	0·5	69·6	0·126
□	0·5	106·6	0·173

by figure 11. The velocity of the reference frame or convection velocity,

$$U_c = d\xi_1/d\tau_c,$$

is shown as a function of ξ_1/δ^* by figure 12. As previously found by Bull & Willis (1961) and Willmarth & Wooldridge (1962), U_c/U_0 increases with increasing spatial separation. Its asymptotic values from the present data are 0·53 at small ξ_1 and 0·825 at large ξ_1 (compared with 0·56 and 0·83 respectively measured by Willmarth & Wooldridge (1962)). Figure 12 also shows values of the average

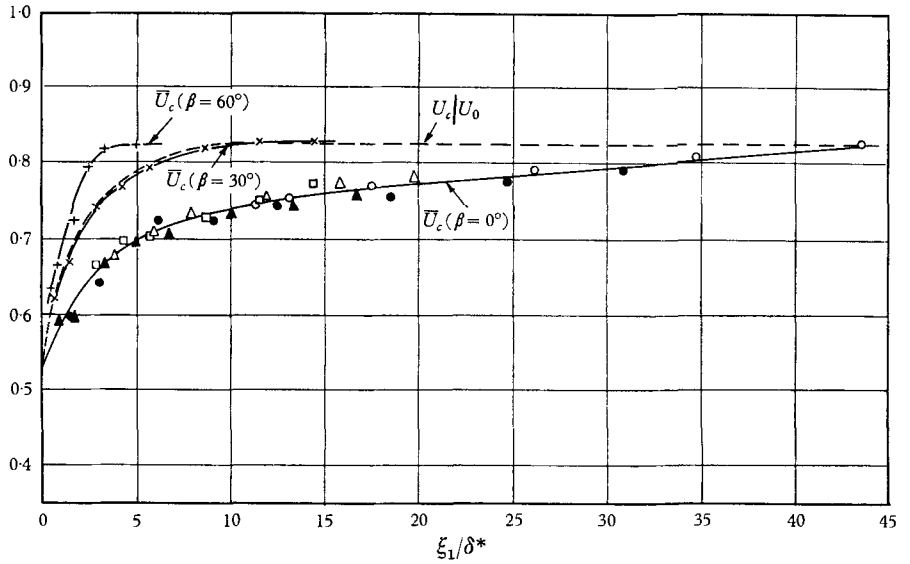

FIGURE 12. Variation of broad-band convection velocity with spatial separation and correlation direction.

	M_0	X (in.)	δ^* (in.)	β
●	0·3	41·6	0·081	0°
▲	0·3	87·6	0·149	0°
×	0·3	87·6	0·149	30°
+	0·3	87·6	0·149	60°
○	0·5	22·6	0·057	0°
△	0·5	69·6	0·126	0°
□	0·5	106·6	0·173	0°

convection velocity $\overline{U}_c = \xi_1/\tau_c$ for comparison with the corresponding values derived from correlations $R_{pp}(\xi\cos\beta, \xi\sin\beta, \tau)$ (where ξ is the magnitude of the separation vector) with $\beta = 30°$ and $\beta = 60°$. The behaviour is similar to that for $\beta = 0°$ just discussed, but with the important difference that the rate of the initial increase with increasing ξ_1/δ^* becomes progressively greater as β increases, that is as the value of ξ_3/δ^* for a given ξ_1/δ^* increases. The asymptotic value of $\overline{U}_c/U_0$ at small separations is not well defined in either of these cases but the asymptotic value at large separations is virtually the same as that for $\beta = 0°$, namely 0·82 to 0·83.

The rate at which the pressure correlation, as seen by an observer moving at U_c, falls off as distance from the initial point of observation increases is shown by the plot of $R_{pp}(\xi_1, 0, \tau_c)$ against ξ_1/δ^*, figure 13. In contrast to the case of the convection velocities, δ^* does not seem to be a good choice of length scale. Figure 13 shows that, for a given ξ_1/δ^*, $R_{pp}(\xi_1, 0, \tau_c)$ falls off with increasing δ^* or Reynolds number. The results of Willmarth (1959) and Wilmarth & Wooldridge (1962), also shown in figure 13, tend to conform to this Reynolds number trend. The effect of Reynolds number would be accentuated if δ were used as the length scale instead of δ^*, which suggests that the scale for the case of the pressure field dominated by motion close to the wall in the inner part of the constant

stress layer, namely ν/U_τ, might be more appropriate. Therefore the data have also been shown as a function of $\xi_1 U_\tau/\nu$ in figure 13. They still show some scatter but the collapse is considerably better than that obtained in terms of ξ_1/δ^* although now the Reynolds number trend, at least in the present data,

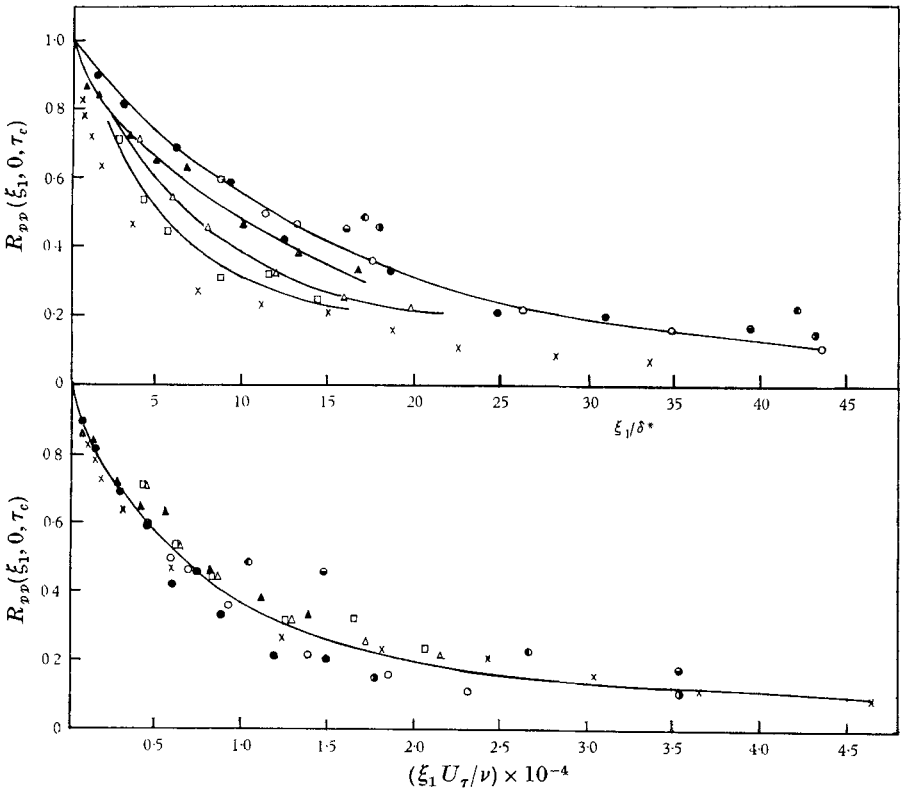

FIGURE 13. Longitudinal correlation in a reference frame moving at convection velocity.

	M_0	δ^* (in.)	Re_{δ^*}	
●	0·3	0·081	13,700	Present data
▲	0·3	0·149	25,400	
○	0·5	0·057	15,100	
△	0·5	0·126	33,300	
□	0·5	0·173	45,700	
◑	0·333	0·070	11,000	Willmarth (1959)
◐	0·465	0·073	19,000	
◒	0·672	0·078	28,000	
×	0·180	0·041	49,500	Willmarth & Wooldridge (1962)

has been slightly reversed. If U_τ/U_0 is taken to be proportional to $Re_\delta^{-\frac{1}{8}}$ (where $Re_\delta = U_0\delta/\nu$), ξ_1/δ^* is proportional to $(\xi_1/\delta)Re_\delta^{\frac{1}{8}}$ (since in the case of a self-preserving velocity profile δ^*/δ is proportional to U_τ/U_0) while $\xi_1 U_\tau/\nu$ is proportional to $(\xi_1/\delta)Re_\delta^{\frac{7}{8}}$; the present data would lie fairly well on a single curve if plotted against a parameter with an intermediate form of Reynolds number dependence such as $(\xi_1/\delta)Re_\delta^{\frac{3}{4}}$ although they would not then be so consistent with the data of Willmarth.

6. Narrow-band measurements

6.1. *Correlation of filtered pressure signals*

The various frequency or wave-number components which make up the pressure field can be examined by filtering the pressure signals into narrow frequency bands and making correlation measurements on the resulting signals.

Let $p(\mathbf{x},t\|\omega)$ be the signal obtained by passing the output from a pressure transducer at $\mathbf{x}$ through an ideal filter which has a narrow pass band, centred on frequency ω and of width $\Delta\omega$. If the pressure field is considered homogeneous and stationary the space–time covariance of two such signals (from identical filters) $\langle p(\mathbf{x},t\|\omega)\,p(\mathbf{x}+\boldsymbol{\xi},t+\tau\|\omega)\rangle$ can be written as $Q_{pp}(\xi_1,\xi_3,\tau\,\|\omega)$, a function of the separation variables and ω only. It can be shown (see, for example, Bull 1961; Corcos 1962) that

$$Q_{pp}(\xi_1,\xi_3,\tau\|\omega) = 2|\phi_{pp}(\xi_1,\xi_3,\omega)|\cos(\omega\tau+\alpha)\,\Delta\omega, \tag{2}$$

where

$$\phi_{pp}(\xi_1,\xi_3,\omega) = |\phi_{pp}(\xi_1,\xi_3,\omega)|e^{i\alpha}$$

is the cross-spectral density of the pressure fluctuations, a partial Fourier transform of the broad-band space–time covariance given by the relations

$$\phi_{pp}(\xi_1,\xi_3,\omega) = \frac{1}{2\pi}\int_{-\infty}^{\infty} Q_{pp}(\xi_1,\xi_3,\tau)\,e^{-i\omega\tau}\,d\tau, \tag{3}$$

$$Q_{pp}(\xi_1,\xi_3,\tau) = \int_{-\infty}^{\infty} \phi_{pp}(\xi_1,\xi_3,\omega)\,e^{i\omega\tau}\,d\omega. \tag{4}$$

The covariance of (2) can be converted to a correlation coefficient

$$R_{pp}(\xi_1,\xi_3,\tau\|\omega)$$

which is independent of the filter bandwidth by dividing it by the mean-square filtered signal, $Q_{pp}(0,0,0\|\omega)$ or $2\phi_{pp}(0,0,\omega)\,\Delta\omega$. (Note that $2\phi_{pp}(0,0,\omega)$ is the frequency power spectral density $\phi_p(\omega)$ as previously defined.) Thus

$$R_{pp}(\xi_1,\xi_3,\tau\|\omega) = \frac{|\phi_{pp}(\xi_1,\xi_3,\omega)|\cos(\omega\tau+\alpha)}{\phi_{pp}(0,0,\omega)}. \tag{5}$$

Particular cases of (3), those for which $\tau = 0, \pi/2\omega$, were used by Harrison (1958) as the basis of measurement of the real and imaginary parts of the longitudinal cross-spectral density.

In the present experiments, measurements were made of the amplitude of the narrow-band correlation coefficient, that is of

$$|R_{pp}(\xi_1,\xi_3,\tau\|\omega)| = |\phi_{pp}(\xi_1,\xi_3,\omega)|/\phi_{pp}(0,0,\omega)$$

and of the phase angle α. $|R_{pp}(\xi_1,0,\tau\|\omega)|$ corresponds to the function $A(\xi,\omega)$ used by Corcos (1962). The quantity $|R_{pp}(\xi_1,\xi_3,\tau\|\omega)|^2$ was used by Harrison (1958) as a measure of the 'coherence' of the narrow-band pressure fluctuation at a downstream point with that at an upstream point. The departure of this quantity from unity gives a measure of the intensity of the uncorrelated component developed by the pressure fluctuation in its travel between the two points.

The phase angle has a non-zero value because of the convected nature of the wall-pressure field. It is a function of frequency and is determined by the convection velocity $U_c(\omega)$ of a particular component of the field. For the experimental data to be presented we shall define $U_c(\omega)$ by means of the relation

$$\alpha = -\omega\xi_1/U_c(\omega). \tag{6}$$

In practice, owing to the finite, though small bandwidth of the filters used, the narrow-band correlation coefficient at a given ξ_1 shows a damped sinusoidal variation with τ; the maximum amplitude occurs at $\tau = \xi_1/U_c(\omega)$ and is there equal to the zero bandwidth value given by (5); see Bull (1961) and Corcos (1962).

6.2. *Functional form of the narrow-band space–time correlations*

Before considering the experimental results for the narrow-band space–time correlation function of the wall-pressure field we shall consider possible forms which this function might take.

(i) *'Frozen' pressure pattern*

First, consider a spatial pattern of pressure convected in the x_1-direction, without change, at velocity U_c. The correlation function of such a pattern satisfies the relation

$$Q_{pp}(\xi_1, \xi_3, \tau) = Q_{pp}(\xi_1 - U_c\tau, \xi_3, 0).$$

Substitution of this relation in (3) leads to

$$\phi_{pp}(\xi_1, \xi_3, \omega) = \frac{e^{-i\omega\xi_1/U_c}}{2\pi U_c} \int_{-\infty}^{\infty} Q_{pp}(y, \xi_3, 0)\, e^{i\omega y/U_c} dy.$$

We then have

$$\phi_{pp}(\xi_1, \xi_3, \omega) = \phi_{pp}(0, \xi_3, \omega)\, e^{-i\omega\xi_1/U_c}.$$

Hence by (5) the longitudinal narrow-band correlation coefficient is given by

$$R_{pp}(\xi_1, 0, \tau \| \omega) = \cos(\omega\tau - \omega\xi_1/U_c). \tag{7}$$

Note that the relation between phase angle and convection velocity here is the same as that used to define the experimental value of $U_c(\omega)$, equation (6).

(ii) *Almost frozen pressure field with constant spatial scale*

Suppose that the broad-band correlation of the field relative to a frame of reference moving at a constant speed U_c in the x_1-direction is given by

$$R_M(\xi_1, \xi_3, \tau) = R_\tau(\tau)\, R_\xi(\xi_1, \xi_3), \tag{8}$$

where $R_\tau(0) = R_\xi(0, 0) = 1$. This represents a field which has similar spatial correlation properties at all time delays, the space correlation magnitude simply varying with time delay. (This representation has been previously used by Lilley & Hodgson, 1960.)

Let

$$\left.\begin{aligned} R_\tau(\tau) &= \int_{-\infty}^{\infty} \phi(\omega)\, e^{i\omega\tau}\, d\omega, \\ \phi(\omega) &= \frac{1}{2\pi}\int_{-\infty}^{\infty} R_\tau(\tau)\, e^{-i\omega\tau}\, d\tau, \\ R_\xi(\xi_1, \xi_3) &= \int_{-\infty}^{\infty} \gamma(k_1, \xi_3)\, e^{ik_1\xi_1}\, dk_1, \\ \gamma(k_1, \xi_3) &= \frac{1}{2\pi}\int_{-\infty}^{\infty} R_\xi(\xi_1, \xi_3)\, e^{-ik_1\xi_1}\, d\xi_1. \end{aligned}\right\} \tag{9}$$

For a homogeneous stationary field, $R_\tau(\tau)$ and $R_\xi(\xi_1, \xi_3)$ are real even functions of the variables and hence $\phi(\omega)$ and $\gamma(k_1, \xi_3)$ are both real and are even functions of ω and k_1 respectively. Then we have, using (3) and (9)

$$\begin{aligned} \phi_{pp}(\xi_1, \xi_3, \omega) &= \frac{\langle p^2\rangle}{2\pi}\int_{-\infty}^{\infty} R_\xi\,(\xi_1 - U_c\tau, \xi_3)\, R_\tau(\tau)\, e^{-i\omega\tau}\, d\tau, \\ &= \frac{\langle p^2\rangle}{2\pi}\int_{-\infty}^{\infty} d\tau\, R_\tau(\tau)\, e^{-i\omega\tau}\int_{-\infty}^{\infty} dk_1 \gamma(k_1, \xi_3)\, e^{ik_1(\xi_1 - U_c\tau)}, \\ &= \frac{\langle p^2\rangle}{2\pi}\int_{-\infty}^{\infty} dk_1 \gamma(k_1, \xi_3)\, e^{ik_1\xi_1}\int_{-\infty}^{\infty} d\tau R_\tau(\tau)\, e^{-i(\omega + k_1 U_c)\tau}, \\ &= \langle p^2\rangle \int_{-\infty}^{\infty} \gamma(k_1, \xi_3)\, \phi(\omega + k_1 U_c)\, e^{ik_1\xi_1} dk_1. \end{aligned} \tag{10}$$

Now it will be assumed that the pressure field is almost frozen, that is, that $R_\tau(\tau)$ is a slowly varying function of τ. $\phi(\omega)$ will then have large values over a narrow range of frequencies on either side of zero and will be negligible elsewhere (but the limiting case where $\phi(\omega)$ becomes a delta function is avoided). It will also be assumed that $R_\xi(\xi_1, \xi_3)$ has appreciable values only in the region of $\xi_1 = 0$ (that is, is almost a delta function), so that $\gamma(k_1, \xi_3)$ will be a slowly varying function of k_1. The main contribution to $\phi_{pp}(\xi_1, \xi_3, \omega)$ will then come from wave-numbers in a narrow band centred on $k_1 = -\omega/U_c$ and we may regard $\gamma(k_1, \xi_3)$ as constant over this band with the value $\gamma(-\omega/U_c, \xi_3)$ (or $\gamma(\omega/U_c, \xi_3)$ since γ is an even function of ξ_1). We can then approximate to (10) by

$$\begin{aligned} \phi_{pp}(\xi_1, \xi_3, \omega) &= \langle p^2\rangle \gamma(\omega/U_c, \xi_3)\int_{-\infty}^{\infty} \phi(\omega + k_1 U_c)\, e^{ik_1\xi_1} dk_1, \\ &= \frac{\langle p^2\rangle}{U_c}\gamma(\omega/U_c, \xi_3)\, R_\tau\,(\xi_1/U_c)\, e^{-i\omega\xi_1/U_c}. \end{aligned}$$

Hence $\alpha = -\omega\xi_1/U_c$ and

$$R_{pp}(\xi_1, \xi_3, \tau\|\omega) = \frac{\gamma(\omega/U_c, \xi_3)}{\gamma(\omega/U_c, 0)} R_\tau(\xi_1/U_c)\cos(\omega\tau - \omega\xi_1/U_c). \tag{11}$$

In particular, the longitudinal correlation coefficient is

$$R_{pp}(\xi_1, 0, \tau\|\omega) = R_\tau(\xi_1/U_c)\cos(\omega\tau - \omega\xi_1/U_c). \tag{12}$$

This result was previously derived by Bull (1961). It should be noted that, in the separable variables form assumed for the correlation coefficient referred to a moving reference frame (8), the shapes of the space–time correlation curves

remain similar at all times and therefore the model cannot take account of any variation in the rate of loss of coherence with scale of the components of the pressure field.

(iii) *Field for which spatial pattern is not similar at all stages of evolution*

Previous experimental investigations of the longitudinal cross-spectral density (for example Harrison 1958) have indicated, at least over part of the frequency range, a functional dependence of the form

$$R_{pp}(\xi_1, 0, \tau \| \omega) = A(\omega\xi_1/U_c)\cos(\omega\tau - \omega\xi_1/U_c),$$

which implies that the smaller the wavelength of a pressure field component the faster it loses coherence. For this type of relationship to hold at small values of $\omega\xi_1/U_c$ it would be necessary for $|R_{pp}(\xi_1, 0, \tau\|\omega)|$ to approach unity both as $\xi_1 \to 0$ at finite ω and as $\omega \to 0$ at finite ξ_1. The first of these conditions is automatically satisfied since the correlation amplitude must tend to unity as $\xi_1 \to 0$ no matter what the value of ω and no matter what the form of the function A. But, if $|R_{pp}(\xi_1, 0, \tau\|\omega)|$ were to tend to unity as $\omega \to 0$ even at finite ξ_1, this would imply that the low-frequency components of the wall pressure were coherent over very large distances, which in turn (following the argument of Fisher & Davies 1964) would lead to the anomalous conclusion that the turbulent motion in the boundary layer which gives rise to these pressure fluctuations is almost unaffected by the mean shearing motion. Thus the relationship cannot be expected to apply at low frequencies while ξ_1 remains finite. (Fisher & Davies found departures of the correlation amplitude from $\omega\xi_1/U_c$ dependence in jet turbulence.) However, it may be an acceptable asymptotic form for finite and not too small values of $\omega\xi_1/U_c$. Corcos (1962) has suggested that the general form of the narrow-band correlations may be

$$R_{pp}(\xi_1, \xi_3, \tau\|\omega) = C(\omega\xi_1/U_c, \omega\xi_3/U_c)\cos(\omega\tau - \omega\xi_1/U_c), \tag{13}$$

except for small values of $\omega\xi_1/U_c$ and $\omega\xi_3/U_c$ when ξ_1 and ξ_3 are non-zero.

6.3. *Experimental results*

From curves of the longitudinal correlation coefficient $R_{pp}(\xi_1, 0, \tau\|\omega)$ plotted against time delay (of which figure 14 is typical) values of the correlation amplitude and convection velocity $U_c(\omega)$ (as defined by (6)) were obtained. $U_c(\omega)/U_0$ is shown as a function of $\omega\delta^*/U_0$ in figure 15.† Some experimental scatter is evident. This is probably partly due to the difficulty of accurately phase matching the $\frac{1}{3}$-octave filters, especially at the lower frequencies. The results are in fair agreement with the boundary-layer data of Willmarth & Wooldridge as given by Corcos (1963*b*). Corcos's pipe flow convection velocities (Corcos 1963*b*) are in general about $0{\cdot}1U_0$ greater than the boundary-layer data. Figure 15 also shows convection velocities determined from correlations for $\beta = 30°$ and 60°. There is considerably more experimental scatter here, particularly in the 60° case, where the time delays are very much smaller than for the same ξ in the stream direction.

† Note that the convection velocity data previously given in figure 18 of *AGARD Report* 455 have since been found to be in error at the two smallest spatial separations.

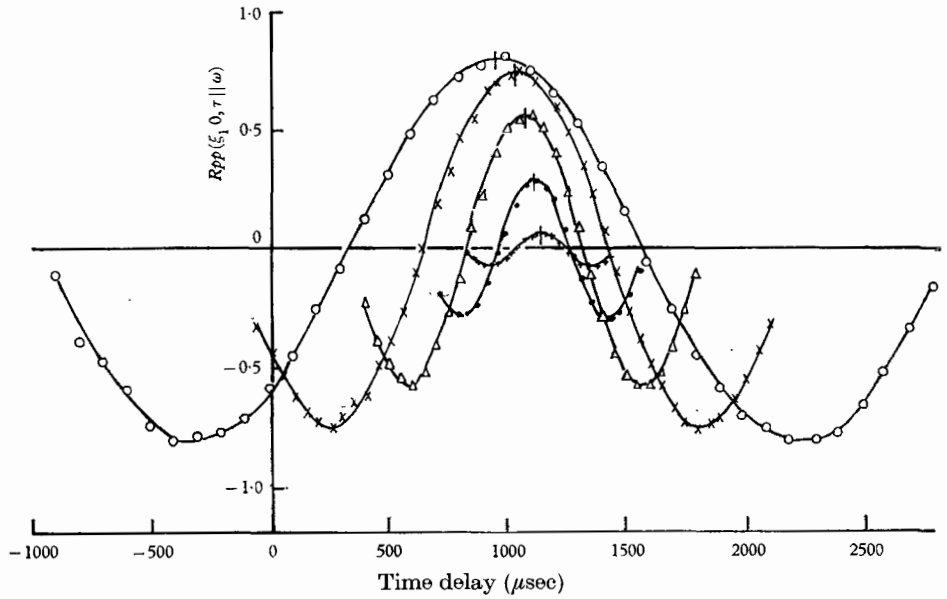

FIGURE 14. Typical narrow-band longitudinal space–time correlations $M_0 = 0{\cdot}3$, $\delta^* = 0{\cdot}149$ in., $\xi_1/\delta^* = 5{\cdot}00$. Frequency at 3·75 in./sec replay speed: ○, 400 c/s; ×, 630 c/s; △, 1000 c/s; ●, 1600 c/s; +, 2500 c/s.

However, the convection velocities are essentially the same as those for $\beta = 0°$. The mean $\beta = 0°$ curve of figure 15 was used in obtaining transducer size corrections to root-mean-square pressure and frequency power spectral density (§5.2).

The interesting feature of the behaviour of $|R_{pp}(\xi_1, 0, \tau \| \omega)|$ (figure 16*a*) is that for a given ξ_1/δ^* it is independent of frequency at sufficiently low frequencies, while at the higher frequencies it depends only on the non-dimensional parameter $\omega\xi_1/U_c(\omega)$. The curve for high frequencies can be fairly well represented by

$$|R_{pp}(\xi_1, 0, \tau \| \omega)| = \exp\{-0{\cdot}1\omega\xi_1/U_c(\omega)\}. \tag{14}$$

The amplitude of the lateral correlation $|R_{pp}(0, \xi_3, \tau \| \omega)|$ (figure 16*b*) shows similar behaviour, being independent of frequency at low frequencies and a function of $\omega\xi_3/U_c(\omega)$ at the higher frequencies. The asymptotic high-frequency curve can be quite accurately represented by

$$|R_{pp}(0, \xi_3, \tau \| \omega)| = \exp\{-0{\cdot}715\,\omega\xi_3/U_c(\omega)\}. \tag{15}$$

The asymptotic low-frequency correlation amplitudes are plotted in figure 17.

Values of $|R_{pp}(\xi_1, \xi_3, \tau \| \omega)|$ along lines at angles of $\beta = 30°$ and $60°$ to the stream direction, that is for $\xi_1/\xi_3 = \sqrt{3}$ and $1/\sqrt{3}$ respectively, are plotted against $\omega\xi_1/U_c(\omega)$ in figure 18. Values of $U_c(\omega)$ taken from the mean curve of figure 15 have been used in forming the abscissae. The data are compared with curves obtained by taking the products of values from the asymptotic curves for the longitudinal and lateral correlation amplitudes. As in the longitudinal and lateral cases the points tend to fall on a common curve at higher values of $\omega\xi_1/U_c(\omega)$

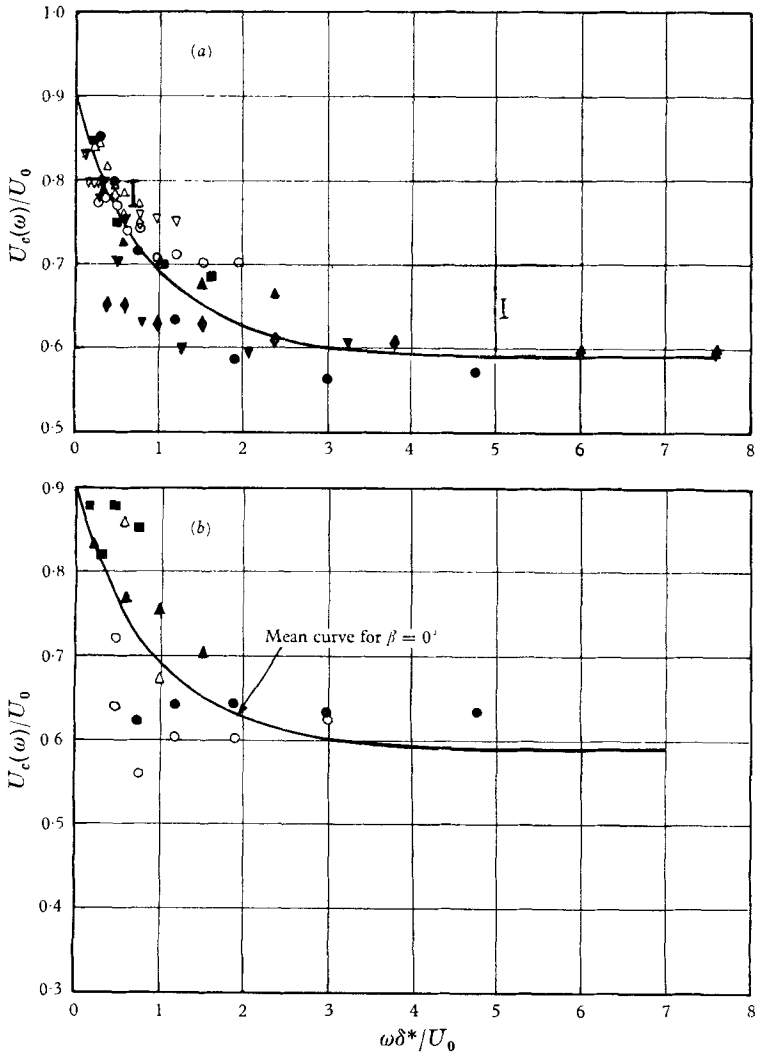

FIGURE 15. Narrow-band convection velocities. (*a*) $\beta = 0$.

	M_0	δ^*	ξ_1/δ^*
◆	0·3	0·149	0·82
●	0·3	0·149	1·66
▼	0·3	0·081	3·07
▲	0·3	0·149	5·00
■	0·3	0·081	9·24
○	0·5	0·126	7·93
◇	0·5	0·126	11·91
▽	0·5	0·126	15·82
△	0·5	0·126	19·75

I Willmarth & Wooldridge (1962) as given by Corcos (1963*b*).

(*b*) $\beta = 30°, 60°$.

	M_0	δ^* (in.)	ξ/δ^*	β
●	0·3	0·149	0·82	30°
▲	0·3	0·149	3·33	30°
■	0·3	0·149	6·72	30°
○	0·3	0·149	0·82	60°
△	0·3	0·149	3·33	60°

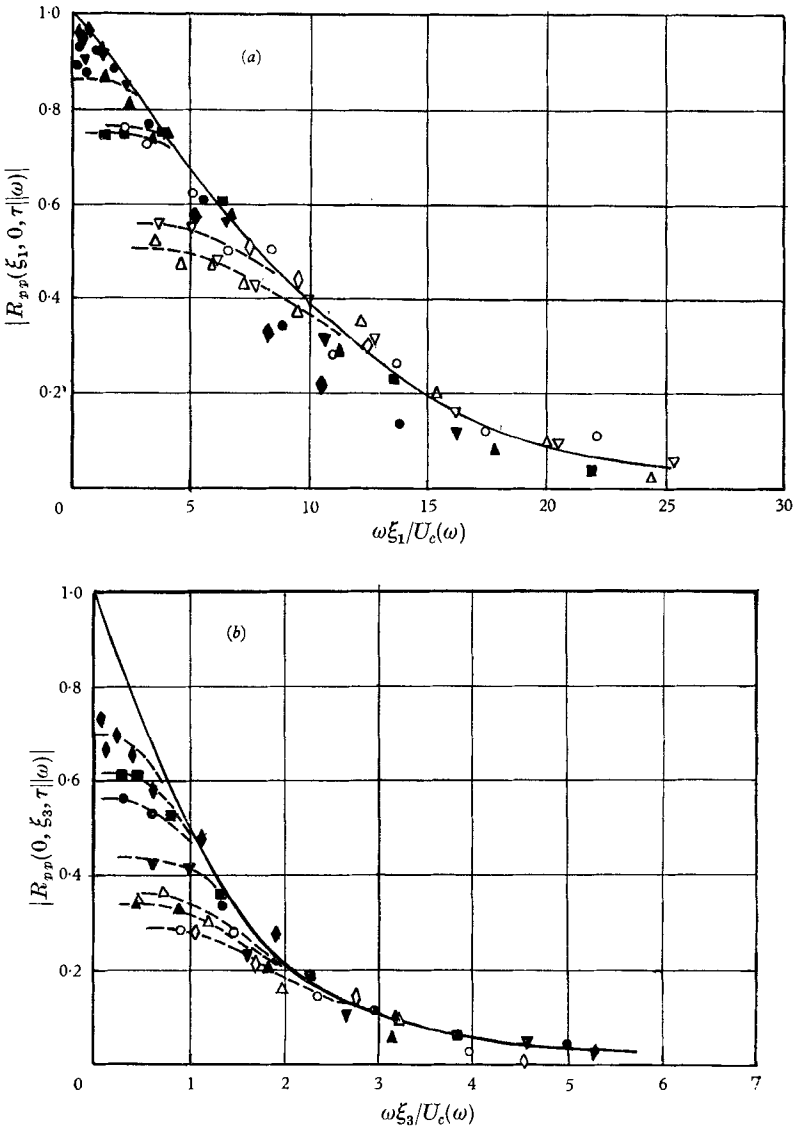

FIGURE 16. Amplitude of narrow-band space–time correlations. (*a*) Longitudinal ($\beta = 0°$); see figure 15*a* for notation. (*b*) Lateral ($\beta = 90°$).

	M_0	δ^* (in.)	ξ_3/δ^*
◆	0·3	0·149	0·82
■	0·3	0·081	1·52
●	0·3	0·149	1·66
▼	0·3	0·081	3·07
▲	0·3	0·149	5·00
△	0·5	0·126	3·96
○	0·5	0·126	7·90
◇	0·5	0·126	11·86

but depart from it at low values. However, there are fewer data in this case and the effects are not so well defined. The relation

$$|R_{pp}(\xi_1, \xi_3, \tau\|\omega)| = |R_{pp}(\xi_1, 0, \tau\|\omega)| \times |R_{pp}(0, \xi_3, \tau\|\omega)|$$

seems to give a reasonable approximation to the observed values.

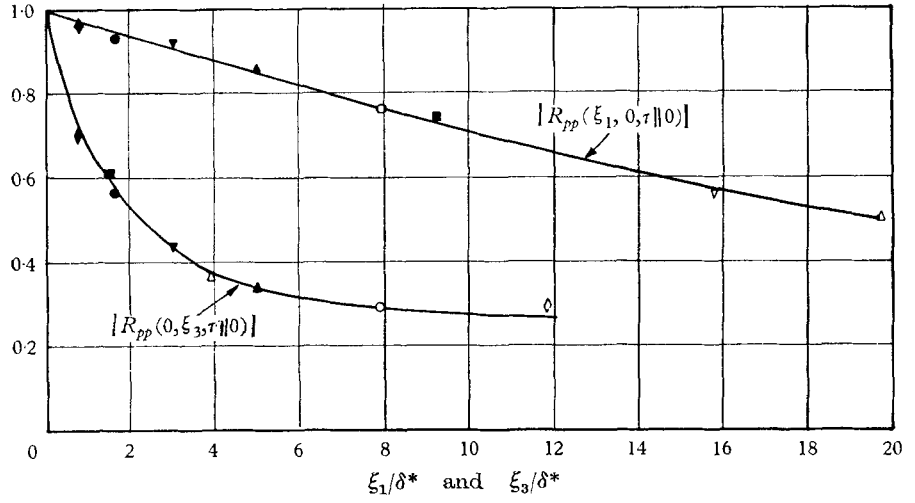

FIGURE 17. Asymptotic values of narrow-band space–time correlation amplitudes at low frequencies.

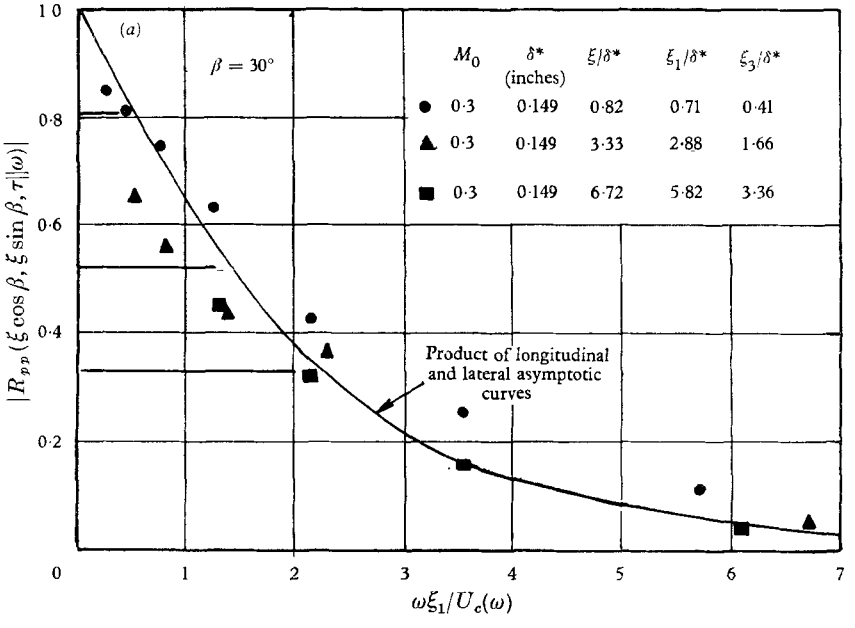

FIGURE 18*a*. For legend see facing page.

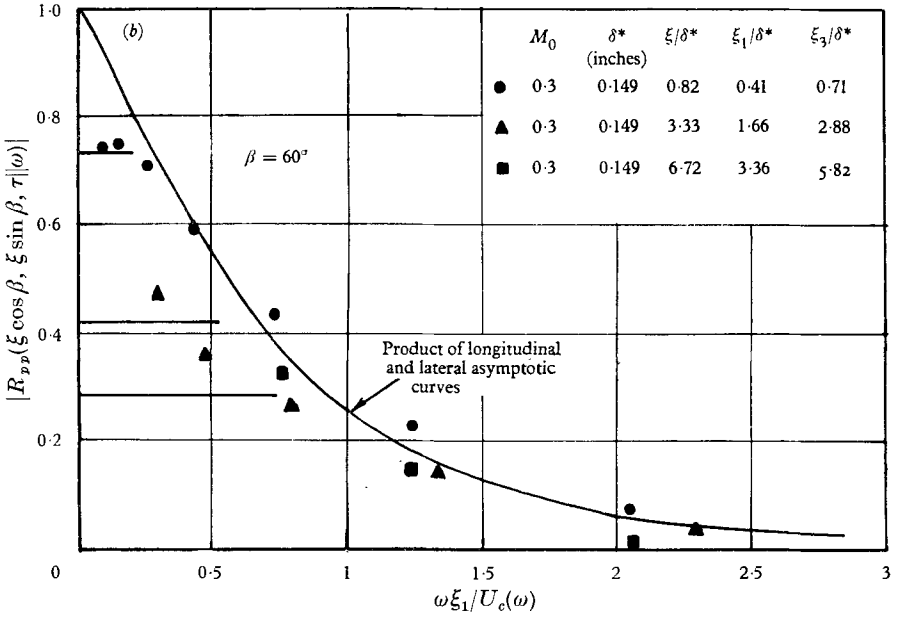

FIGURE 18. Amplitude of narrow-band space–time correlations (*a*) $\beta = 30°$, (*b*) $\beta = 60°$.

6.4. *Calculation of broad-band correlations from narrow-band results*

The extent to which the narrow-band correlation coefficient can be represented by a function of the parameters $\omega\xi_1/U_c(\omega)$ and $\omega\xi_3/U_c(\omega)$ only will now be briefly examined. This form has been used extensively by Corcos (1962) as a basis for calculating broad-band space–time correlations of the pressure field from narrow-band data. If the narrow-band correlation coefficient is given by (13) then the broad-band covariance is given by

$$Q_{pp}(\xi_1, \xi_3, \tau) = \int_0^\infty \phi_p(\omega)\, C(\omega\xi_1/U_c(\omega), \omega\xi_3/U_c(\omega)) \cos(\omega\tau - \omega\xi_1/U_c(\omega))\, d\omega. \quad (16)$$

As illustrations, only the two particular cases of the longitudinal and lateral space correlations will be considered. If $C(\omega\xi_1/U_c(\omega), 0)$ is represented by

$$\exp(-c_1\omega\xi_1/U_c(\omega))$$

as in (14) and $C(0, \omega\xi_3/U_c(\omega))$ by $\exp(-c_3\omega\xi_3/U_c(\omega))$ as in (15), and $\phi_p(\omega)$ is also represented by a sum of exponential terms such as $A_n \exp(-a_n\tilde{\omega})$ as in (1) then

$$Q_{pp}(\xi_1, 0, 0)/q_0^2 = \sum_n A_n \frac{a_n + c_1\Gamma_1}{(a_n + c_1\Gamma_1)^2 + \Gamma_1^2}, \quad (17)$$

where $\Gamma_i = U_0\xi_i/U_c(\omega)\,\delta^*$. $\langle p^2\rangle$ is obtained as $Q_{pp}(0, 0, 0)$ and hence $R_{pp}(\xi_1, 0, 0)$ can be calculated. The expression for Q_{pp} (16) is a genuine Fourier transform only if $U_c(\omega)$ is independent of ω. However, although $U_c(\omega)$ does vary with ω a representative constant value can be assigned without introducing appreciable errors. Equation (17) was evaluated using the expression for $\phi_p(\omega)$ given by (1) and assuming a constant convection velocity for each term equal to that corre-

sponding to the $\omega\delta^*/U_0$ at its half-power point ($U_c/U_0 = 0{\cdot}795$, $0{\cdot}653$ and $0{\cdot}865$, for the three terms of (1) respectively). The result is compared with the mean experimental curve in figure 19*a*. The agreement is seen to be quite good. In a similar way

$$Q_{pp}(0, \xi_3, 0)/q_0^2 = \sum_n \frac{A_n}{a_n + c_3 \Gamma_3}. \tag{18}$$

The lateral broad-band correlation calculated from this expression is compared with the experimental mean line in figure 19*b*. The agreement is very good.

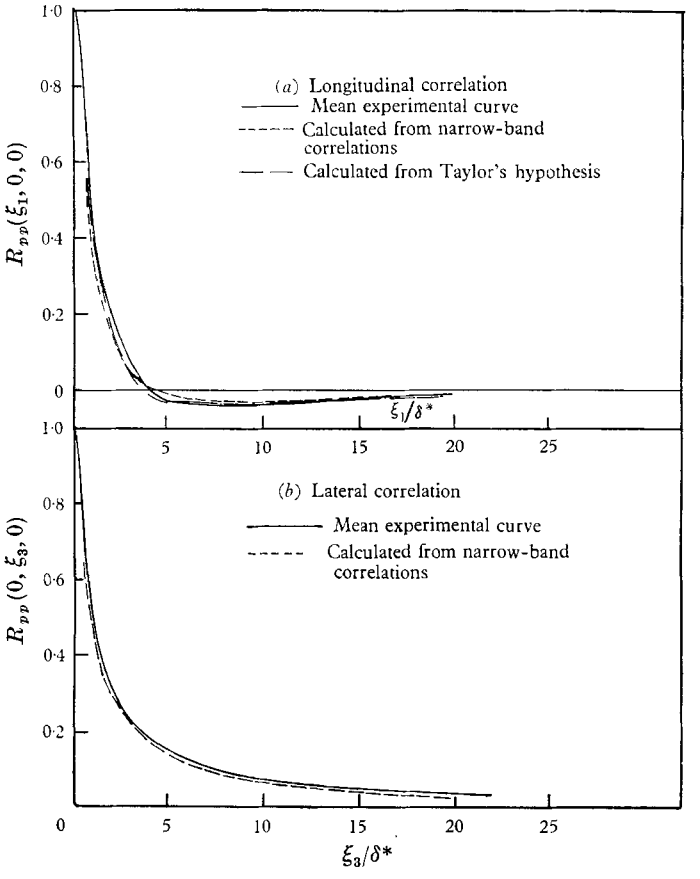

FIGURE 19. Comparison of measured broad-band space correlations with calculations based on Taylor's hypothesis and narrow-band data.

Good agreement would be expected at close spacings where the broad-band correlation coefficient is high, because then $\omega\xi_1/U_c(\omega)$ and $\omega\xi_3/U_c(\omega)$ dependence extends down to very small values of the frequency parameters. However, at larger spacings where this dependence breaks down over a greater range of values of the parameters, whereas the relative errors introduced tend to be larger, the corresponding correlation coefficients are much smaller, and the rather large relative errors give rise to fairly small absolute errors. The net effect is a fairly good reproduction of the broad-band correlation over the whole separation range.

7. Discussion

7.1. *Equivalence of frequency and longitudinal wave-number components*

It has been assumed on several occasions in this paper that a fixed-point frequency component of the wall-pressure field arises from convection of a corresponding longitudinal wave-number component of the pressure field (Taylor's hypothesis) according to the relation $\omega = k_1 U_c(k_1)$. Justification of this assumption requires that the various wave-number components behave essentially as if they were frozen, and that a unique convection velocity can be associated with a given wave-number so that a particular frequency is due to one wave-number (or a narrow band of wave-numbers) and not a wide range of wave-numbers with a wide range of convection velocities for which the product $k_1 U_c$ is constant. Figure 15 shows that within fairly narrow limits (in general better than $\pm 10\,\%$) it is possible to associate a unique value of $U_c(\omega)/U_0$ with a given Strouhal number $\omega\delta^*/U_0$ and hence, if the components are very nearly frozen, with a given value of $k_1\delta^*$. The degree to which the various wave-number components behave as if they were frozen can be gauged by comparing the broad-band space correlation, calculated from the frequency power spectral density on the basis of this assumption, with the corresponding experimental result. For frozen wave-number components

$$\begin{aligned} Q_{pp}(\xi_1, 0, 0)/q_0^2 &= \left[\int_{-\infty}^{\infty} \phi_{pp}(0, 0, \omega)\, e^{i\omega\tau} d\omega\right]_{\tau = -\xi_1/U_c(\omega)}, \\ &= \int_0^{\infty} \phi_p(\omega) \cos \omega\xi_1/U_c(\omega)\, d\omega, \\ &= \sum_n \frac{A_n a_n}{a_n^2 + \Gamma_1^2}, \end{aligned}$$

if $\phi_p(\omega)$ is given by (1). Figure 19(*a*) shows the comparison between calculation and experiment. There is quite good agreement between the two, indicating that it is an acceptable approximation to identify fixed-point frequencies with longitudinal wave-numbers.

7.2. *Location of pressure sources*

If, as discussed above, the narrow-band convection velocity is a function of the non-dimensional wave-number $k_1\delta^*$ only and it is assumed that velocity disturbances in the boundary layer are convected at local mean flow velocity (as indicated by the measurements of u_1 spectra and pressure–velocity correlations made by Wooldridge & Willmarth (1962)) then the fluctuating pressure components of a given frequency or longitudinal wave-number can be associated approximately with velocity disturbances whose 'centre of gravity' is at the particular distance from the wall where the mean velocity is equal to $U_c(\omega)$. Similarly the centre of gravity of disturbances repsonsible for the broad-band correlations can be located where the mean velocity is equal to the observed broad-band convection velocity.

At very small separations where the broad-band convection velocity U_c approaches $0{\cdot}53U_0$ the x_2 value for the present experiments is in the range

$35 < x_2 U_\tau/\nu < 70$ ($0{\cdot}015 > x_2/\delta > 0{\cdot}006$) depending on the Reynolds number (possible effects of Reynolds number on U_c which could only be investigated by very much more detailed experiments are neglected here). This implies that at these separations the wall-pressure field receives important contributions from sources in the transition region (usually taken as $5 < x_2 U_\tau/\nu < 30$) between the viscous sublayer and the fully turbulent part of the constant stress layer and also from the inner part of the latter, as well as from sources further out in the boundary layer.

On the other hand the asymptotic value of the narrow-band convection velocity at high frequencies is $0{\cdot}59U_0$, which would locate the centre of gravity of the velocity disturbances giving rise to the highest-frequency pressure components at an $x_2 U_\tau/\nu$ value depending on Reynolds number of from 70 to 150 ($x_2/\delta = 0{\cdot}030$ to $0{\cdot}013$), rather further from the wall than indicated by the broad-band data. Although the difference of about 10 % in the two convection velocities can probably be partly accounted for by experimental errors and the different methods of defining convection velocity in the two cases, the broad-band convection velocity (which might if anything have been expected to be the higher since it contains some contributions from large-scale (faster moving) as well as small-scale turbulence) is subject to additional errors from the process of extrapolating the space–time graph (figure 11) to the origin and taking the slope there, and the value obtained may therefore be too low (compare $0{\cdot}56U_0$ obtained by Willmarth & Wooldridge 1962). However, the results clearly point to the fine-scale motion in the innermost part of the fully turbulent region of the constant stress layer as an important source of wall-pressure fluctuations. It seems likely that sources in the transition region also make a significant contribution but because of the apparent inconsistencies in the data it is not possible to be so definite on this point.

The fact that the broad-band convection velocity approaches $0{\cdot}825U_0$ at large separations suggests that at this stage the correlation is due to eddy systems with centre of gravity at $0{\cdot}25$ to $0{\cdot}31\,\delta$ (i.e. just outside the constant stress layer) but fairly widely distributed throughout the boundary layer with an important contribution from the large-eddy structure of the layer. Since the narrow-band convection velocity appears not to exceed $0{\cdot}9U_0$ it seems that eddy systems whose centres of gravity are located further from the wall than about $0{\cdot}5\delta$ make no significant contribution to the wall-pressure fluctuations.

7.3. *Division of the field into two wave number families*

The variation of the amplitude of the narrow-band longitudinal and lateral correlations with frequency and spatial separation (figure 16) suggests that the pressure field comprises two families of wave-number components, one of high wave-number components which lose coherence with $\omega\xi_1/U_c(\omega)$ and $\omega\xi_3/U_c(\omega)$ similarity (as in case 3 of §6.2), and the other of low wave-number components which lose coherence as a group independently of wave-number (as in case 2 of §6.2).

Divergence from $\omega\xi_1/U_c(\omega)$ and $\omega\xi_3/U_c(\omega)$ similarity occurs at higher values of these parameters the greater the separation, but always at roughly the same value

of $\omega\delta^*/U_c(\omega)$. Thus the division between the two families can be characterized by the Strouhal number at which the curve of correlation amplitude for the high wave-number similarity region has a value equal to the limiting low-frequency value; that is $|R_{pp}(\xi_1, 0, \tau\|0)|$ or $|R_{pp}(0, \xi_3, \tau\|0)|$ at a given separation. (This Strouhal number has the advantage that it can be readily obtained but it does represent a somewhat low estimate of the dividing Strouhal number.) Both the longitudinal and lateral correlations give values which are very nearly constant over the range of separation investigated. In both cases the average value is $\omega\delta^*/U_c(\omega) = 0{\cdot}36$. This corresponds to a wavelength λ_1 in the stream direction of $2\pi\delta^*/0{\cdot}36 = 17{\cdot}4\delta^*$ or about 2δ. The convection velocity for this wavelength is about $0{\cdot}81U_0$† so that in terms of distance from the wall the division between the two families occurs, depending on Reynolds number, in the region of $x_2 = 0{\cdot}20$–$0{\cdot}27\delta$ or somewhat closer to the wall. Thus the high wave-number family of pressure eddies results from motion in the constant stress layer while the low wave-number family is due to the outer region of the boundary layer.

It is interesting to note that the demarcation wavelength of about 2δ associates the low wave-number family with the slowly rising low-frequency portion of the frequency power spectrum (figure 5) and the high wave-number family with the high-frequency falling part of the spectrum.

From the spectral curves it can be estimated that the respective contributions to the mean-square pressure of the high and low wave-number families are roughly 75 and 25 %.

For the high wave-number family, $\omega\xi_1/U_c(\omega)$ similarity implies that the various wave-number components lose coherence in times which are proportional to the times required for them to be convected distances equal to their wavelengths. If we consider that a component has lost its identity when the correlation amplitude $|R_{pp}(\xi_1, 0, \tau\|\omega)|$ has fallen to 0·05 then figure 16*a* indicates that this occurs while the component is convected a distance corresponding to

$$\omega\xi_1/U_c(\omega) \simeq 24{\cdot}5 \quad \text{or} \quad \xi_1 \simeq 4\lambda_1.$$

The comparable value found by Harrison (1958) was about 2 wavelengths, while a more recent measurement by Willmarth & Wooldridge (1962) gave 4 to 6 wavelengths. Alternatively we could define an integral coherence length scale given by

$$[\Lambda_1(\omega)]_{pp} = \int_{-\infty}^{\infty} |R_{pp}(\xi_1, 0, \tau\|\omega)|\, d\xi_1.$$

Using (14) the value of this scale is $20U_c(\omega)/\omega$ or $3{\cdot}2\lambda_1$. The coherence length scale is not a length scale in the normal sense but really represents the time scale of coherence of the components when viewed in a frame of reference moving at the convection velocity (that is $3{\cdot}2\lambda_1/U_c(\omega)$).

For the lateral direction $\omega\xi_3/U_c(\omega)$ similarity implies that the various longitudinal wave-number components are laterally coherent over distances proportional to their wavelengths. The behaviour of the broad-band convection velocity for $\xi_3 \neq 0$ (figure 12), which increases more rapidly with increasing ξ_1 than for

† This velocity was incorrectly given in *University of Southampton Report A.A.S.U.* 243.

$\xi_3 = 0$, but approaches the same final values at large ξ_1, is consistent with this. Again taking a correlation amplitude of 0·05 as the criterion, the coherence length is given by $\omega\xi_3/U_c(\omega) = 4{\cdot}7$ or $\xi_3/\lambda_1 \simeq 0{\cdot}75$, that is, 1·5 wavelengths for ξ_3 positive and negative. This figure gives some support to the result found in the broad-band case that the lateral integral scale of the pressure field was greater than the longitudinal. We could also define an integral lateral coherence length scale by

$$[\Lambda_3(\omega)]_{pp} = \int_{-\infty}^{\infty} |R_{pp}(0, \xi_3, \tau\|\omega)| d\xi_3,$$

which from (15) has the value $0{\cdot}45\lambda_1$.

7.4. *Evolution of the pressure field*

The division of the pressure field into two wave-number families with different decay characteristics leads to two stages in the evolution of the field. In the first stage both families make significant contributions to the correlation functions, but the development of the field is more strongly influenced by the high wave-number family associated with motion in the constant stress layer. The property of the high wave-number family that, at small separations, its components lose coherence more rapidly the higher their wave-number, which leads to $\omega\xi_1/U_c(\omega)$ and $\omega\xi_3/U_c(\omega)$ similarity, is dominant. At the same time the spectrum of correlated components is becoming progressively curtailed at high wave-numbers as separation increases. This is evident in the variation with spatial separation of the broad-band convection velocity and longitudinal space–time correlations. At small separations the latter have sharp narrow peaks indicating a broad spectrum of correlated wave-numbers, but as separation increases the peaks rapidly disappear and the curves become broader and flatter (see figure 10), indicating a progressive loss of high wave-number contribution. The broad-band convection velocity results already discussed show that initially there is a strong contribution from the innermost part of the fully turbulent region of the constant stress layer and possibly the transition region also, but as spatial spearation increases to a few displacement thicknesses the broad-band convection velocity rises rapidly towards the asymptotic value $0{\cdot}825U_0$ characteristic of the large-scale structure of the field, indicating that the contribution to the pressure correlation from the fine-scale motion in this region close to the wall quickly becomes small, owing to the rapid dissipation and dispersion of pressure sources by the high shear occurring there. However, there are indications that motion not too far from the wall influences the pressure field up to quite large separations; the variation of broad-band convection velocity suggests that the influence of the high wave-number family persists for the time taken for it to be convected a distance of at least $10\delta^*$, while the dependence of the moving-frame correlation $R_{pp}(\xi_1, 0, \tau_c)$ on the length scale ν/U_τ (figure 13) indicates that some influence persists over a convection distance of at least $20\delta^*$ or about $2{\cdot}4\delta$.

As the high-frequency components lose coherence the correlation becomes increasingly dominated by the low wave-number family. In this second stage the

development of the field is due to loss of coherence of the components of this family with spectral similarity. This view is supported by the observations that at the larger separations the broad-band convection velocity U_c is independent of separation (so that the correlated components arise from turbulence which has the same centre of gravity at all times in this stage); that the broad-band space–time correlation curves are roughly similar at large separations, increasing separation serving to reduce their magnitude without large changes in correlation scale; and that the narrow-band measurements show coherence of the low wave-number family to be independent of frequency.

Since the narrow-band convection velocities are essentially the same for $\beta = 0°$, $30°$ and $60°$ the various components of the pressure field apparently do not undergo any rapid distortion in the lateral direction during convection, retaining the same convection velocity at all locations across their width. This indicates that, as might be expected, dispersion of pressure sources occurs almost entirely through the action of the relative shearing motion of the mean flow at different distances from the wall.

The author wishes to express his appreciation to Prof. E. J. Richards for his interest in the work reported, and to the many members of the Department of Aeronautics and Astronautics in the University of Southampton (where the work was done) who assisted with the construction of apparatus, processing of data and preparation of diagrams. Financial assistance from the United States Air Force under Contract No. AF 61(052)-358 is also gratefully acknowledged.

REFERENCES

ALLCOCK, G. A., TANNER, P. L. & MCLACHLAN, K. R. 1962 *University of Southampton Rept. A.A.S.U.* 205.

BAKEWELL, H. P., CAREY, G. F., LIBUHA, J. J., SCHLOEMER, H. H. & VON WINKLE, W. A. 1962 *U.S. Navy Underwater Sound Laboratory Rept.* no. 559, 1-052-00-00.

BULL, M. K. 1960 *University of Southampton Rept. A.A.S.U.* 149.

BULL, M. K. 1961 *University of Southampton Rept. A.A.S.U.* 200.

BULL, M. K. & WILLIS, J. L. 1961 *University of Southampton Rept. A.A.S.U.* 199.

BULL, M. K., WILBY, J. F. & BLACKMAN, D. R. 1963 *University of Southampton Rept. A.A.S.U.* 243.

COLES, D. 1956 *J. Fluid Mech.* **1**, 191.

CORCOS, G. M. 1962 *University of California, Institute of Engineering Res. Rept. Series* 183, no. 2.

CORCOS, G. M. 1963*a* Resolution of pressure in turbulence. *J. Acoust. Soc. Am.* **35**, 192.

CORCOS, G. M. 1963*b* *University of California, Institute of Engineering Res. Rept. Series* 183, no. 4.

FISHER, M. J. & DAVIES, P. O. A. L. 1964 *J. Fluid Mech.* **18**, 97.

HARRISON, M. 1958 *David Taylor Model Basin Rept.* 1260.

HODGSON, T. H. 1962 Ph.D. Thesis, London University.

KISTLER, A. L. & CHEN, W. S. 1962 *J. Fluid Mech.* **16**, 41.

KOBASHI, Y. 1957 *J. Phys. Soc. Japan* **12**, 533.

KRAICHNAN, R. H. 1956*a* *J. Acoust. Soc. Am.* **28**, 64.

KRAICHNAN, R. H. 1956*b* *J. Acoust. Soc. Am.* **28**, 378.

KRAICHNAN, R. H. 1957 *J. Acoust. Soc. Am.* **29**, 65.
LAUFER, J. 1954 *Nat. Adv. Comm. Aero. Wash. Tech. Rept.* no. 1174.
LILLEY, G. M. & HODGSON, T. H. 1960 *AGARD Rept.* 276.
PHILLIPS, O. M. 1954 *ARC* 16,963.
SERAFINI, J. S. 1963 *AGARD Rept.* 453.
SKUDRZYK, E. F. & HADDLE, G. P. 1960 *J. Acoust. Soc. Am.* **32**, 19.
UBEROI, M. S. 1954 *Nat. Adv. Comm. Aero. Wash. Tech. Note* no. 3116.
WILLMARTH, W. W. 1958 *Nat. Adv. Comm. Aero. Wash. Tech. Note* no. 4139.
WILLMARTH, W. W. 1959 *N.A.S.A. Memo* 3-17-59W.
WILLMARTH, W. W. & WOOLDRIDGE, C. E., 1962 *J. Fluid Mech.* **14**, 187.
WILLMARTH, W. W. & WOOLDRIDGE, C. E. 1963 *AGARD Rept.* 456.
WILLMARTH, W. W. & ROOS, F. W. 1965 *J. Fluid Mech.* **22**, 81.
WOOLDRIDGE, C. E. & WILLMARTH, W. W. 1962 *University of Michigan Rept.* 02920-2-T.